Università degli Studi di Padova
Padova (Italy), 2021

UNIVERSITÀ
DEGLI STUDI
DI PADOVA

Fluid dynamic analysis and development of a 1 N bipropellant liquid rocket combustion chamber

Candidate: Matteo Zheng

Supervisor: Prof. Francesco Barato
Joint supervisor: Prof. Daniele Pavarin

Master thesis
M.Sc. in Aerospace Engineering

Tesi magistrale
Laurea Magistrale in Ingegneria aerospaziale

DIPARTIMENTO DI INGEGNERIA INDUSTRIALE
Anno accademico 2020-21

Abstract

The New space economy is calling for high performance miniaturized engines to make small satellites capable of performing some high-value missions. When time to orbit is a primary concern, bipropellant chemical engines are a very suitable solution. There are many issues when trying to scale down chemical rocket engines, especially thermal management of the combustion chamber: the heat flux should be minimized to preserve the structural integrity of the engine and to avoid the performance impact of the energy dumped under the form of heat flux at the chamber walls, which is of great relevance for small engines.

Some injection designs have been numerically investigated using RANS CFD methods in order to achieve high combustion efficiency and low convective heat trasfer while being additively manufacturable to reduce costs and the number of parts. Two final designs based on HTP (High-Test Peroxide) as the oxidizer and meeting all these requirements will be presented. One of them is a coaxial non-swirling design with impinging injectors, the other is a moderately swirling design with a central impinging system.

Contents

List of Figures

List of Tables

1 Background: the *New space economy*

1.1 The shift from public to private

In recent years we have seen a rising number of new private companies involved in space activities, from small start-ups with a dozen employees to billion-dollar companies with hefty contracts with NASA. They are working on new telecommunications technologies, navigation and imagery services, biomedical research and most prominently: innovative propulsion systems. Space has not been so exciting since the end of the Cold War and the Space Race. This time the excitement is not coming only from the general public, but from entrepreneurs and non-aerospace corporations as well, indeed some are calling this current trend "the new gold rush" [42] and it is on an international scale.

The STS - Space Transportation System (more commonly known as "Space Shuttle"), although mighty and extremely fascinating on a technical level, had failed in its core objective to reduce the cost to access space. Even in its last years of operation the cost to launch with the STS was actually higher than traditional expendable launchers [1]. The tragedy of Columbia (2003), the second one with fatalities and complete loss of a Shuttle, halted all operations of the STS and in 2004 NASA officially declared their plans of retiring the launcher as soon as possible [41]. This meant the U.S.A. were left unable to send humans and supplies to the ISS (International Space Station) without relying on a third country. The U.S. needed new alternatives, but the government was cautious against funding a new project that could result in the same overspending that happened with the STS, instead they had NASA give contracts to private corporations for the resupply and crew transportation missions to the ISS.

The first wave of contracts was named the Commercial Resupply Services program and it resulted in SpaceX and Orbital Sciences being awarded in 2008 the contracts to resupply the ISS, with these funds they developed respectively the Dragon and Cygnus cargo spacecrafts. A few years later, in 2014, NASA contracted SpaceX and Boeing to develop also human transport modules, in the Commercial Crew Program. In this way the government agency offloaded (to some degree) the economical risk and the technical challenge to multiple private companies, which had to compete and optimize their solutions according to their for-profit nature. The major focus in the cost optimization has been re-usability: in 2010 SpaceX became the first private company to launch and recover a spacecraft (the Dragon cargo module [2], Boeing is also developing a reusable module, named Starliner [17]), later in 2015 their Falcon 9 first stage returned after launch and landed with its own engines, the first time a rocket first stage achieved a powered

vertical landing [5]. This funding of private corporations seems to be paying off: although there have been some delays in development, the costs are turning out much lower than those of the STS: 90 million USD per mission for the Commercial Crew Program [39], while for the STS it was 1.2 billion USD per mission [47]. Europe stepped in recently, with the European Space Agency (ESA) funding 3 start-up companies to develop new compact and cost-effective launchers: Rocket Factory Augsburg, Isar Aerospace and HyImpulse Technologies.

1.2 Small satellites

Another contributing factor for the rise of new players in the space market, and possibly the main one, has been the introduction of very small satellites, which have been possible thanks to the advancements in electronics of the last couple of decades: smaller processors, more energy-dense lithium ion batteries, more efficient triple junction solar panels and smaller sensors [33]. Many objectives that required a classic "medium sized" satellite weighing 500-1000 kg, now can be accomplished by a miniaturized satellite under 100 kg or by a constellation of nanosatellites each under 10kg [28]. These miniaturized satellites can be classified as [28]:

- small satellite (100 - 500 kg)
- microsatellite (10 - 100 kg)
- nanosatellite (1 - 10 kg)
- picosatellite (0.1 - 0.99 kg)

Small satellites in the 100 - 500 kg category can be launched with lower power rockets, which are cheaper to build and operate, leading to substantial cost savings.

Even more cost-effective are the satellites $<$ 100 kg: these satellites can be launched into orbit as a secondary payload of another mission, which usually carries one (or more) larger and heavier satellite, leaving some spare capacity which is sold for a fraction of the cost of the primary contractor(s), this practice is called "rideshare" or "piggyback" launch. However this constrains the launch calendar and the final orbit to those of the primary contractor(s). To solve these issues and to appeal to the new small satellite market segment, some "light" rockets are being developed specifically to be used to launch payloads $<$ 500 kg, like the Electron (already operational) by RocketLab [11] or the LauncherOne by Virgin Galactic [22]. Extremely financially accessible payloads are creating the demand for new launchers, which in turn are bringing down the mission costs and attracting even more investors into the space sector, in a virtuous cycle.

Another cost-saving opportunity was found in standardization: the nanosatellite category is

predominantly represented by the satellites using the modular CubeSat standard (more on this in Chapter 3) and this standardization simplifies the integration into the launcher and the deployment, which in turn reduces development costs [32]. As of January 2021, 1474 nanosats have been launched on orbit (of which 1357 are CubeSats) [18]. Also many CubeSats have made use of COTS (Commercial Off The Shelf) parts to get access to lower cost parts, in place of flight certified parts. This is done where the savings are worth the increase of risk for the mission, which would be unacceptable for a full-sized satellite worth millions of USD.

1.3 Space debris

The Low Earth Orbit (LEO) is crowded with satellites: around 2500 operational and more than 3000 non-operational [16]. The latter falls under the term "space debris" or "space junk", along other objects as: parts of rocket upper stages, residual liquids, explosive bolts, pieces of detached paint, parts of the satellites destroyed in anti-satellite missile tests. The European Space Agency estimates the space debris today consists of more than 34000 objects $>$ 10 cm in size and almost one million with size between 1 cm and 10 cm [21].

Everything in LEO is very slowly decaying due to residual atmospheric drag, but if LEO becomes crowded enough, the impact of a piece of debris with a large satellite at around 8 km/s can be catastrophically destructive, the satellite can break up in many pieces and these can impact another satellite and so on, in a dramatic escalation. This is called the "Kessler syndrome" [35], by the name of the scientist who proposed the theory, and it could render the orbit inoperable for many years should it happen.

The rise in popularity of small satellites needs to counterbalanced by the implementation of de-orbiting systems to be sustainable [8]. New miniaturized propulsion systems for CubeSats could be beneficial for this matter, as their rise in popularity is already causing concern: the current growth is not sustainable without large adoption of mitigation practices [6].

1.4 Current market trends for nanosatellites

Since 2012 the number of nanosatellites launched has shown an almost steady growth, we can see from the figure 1.1 the number of launches in the last four years is ten times what it used to be prior to 2012. The vast majority of these nanosats launched are CubeSats of various sizes, the most popular choices currently being the 3U and 6U configurations [18] (Figure 1.2).

There is a transition from costly large satellites to constellations of numerous nanosatellites whenever the objective allows it. One example is Earth imagery: Planet Labs Inc. decided in

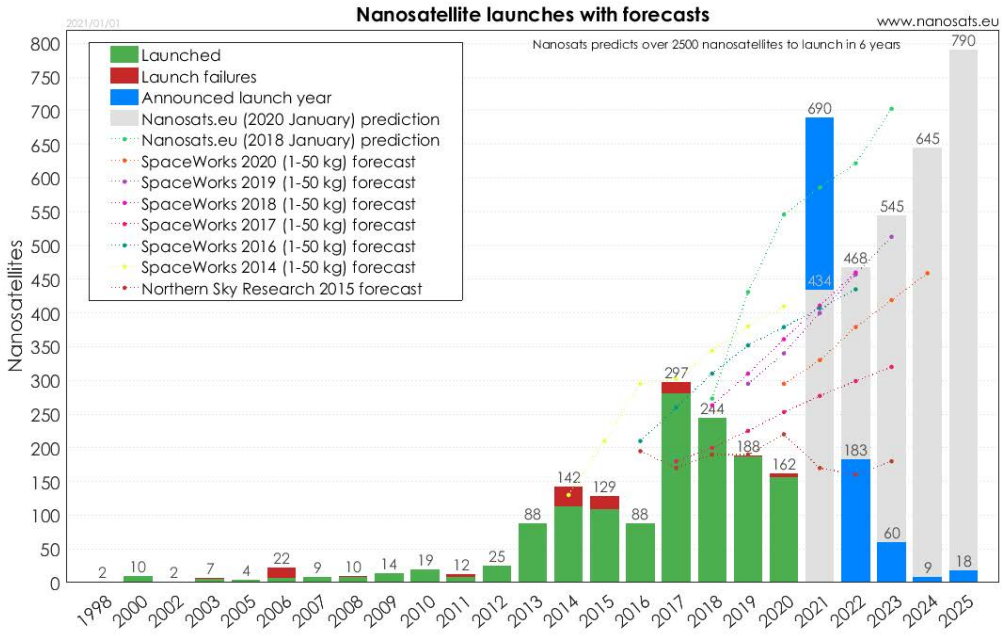

Figure 1.1: Number of nanosatellites launched every year until 2020, with predictions for future years.

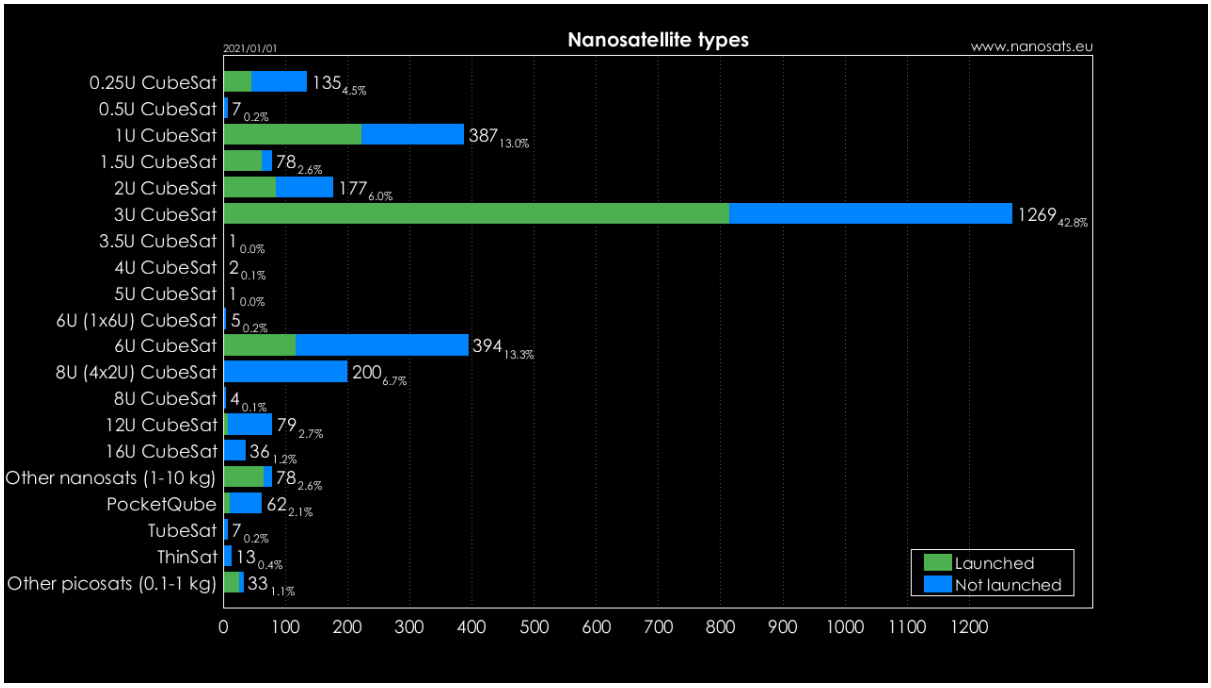

Figure 1.2: Size and format of nanosatellites that have been launched or are programmed to launch, as of January 2021.

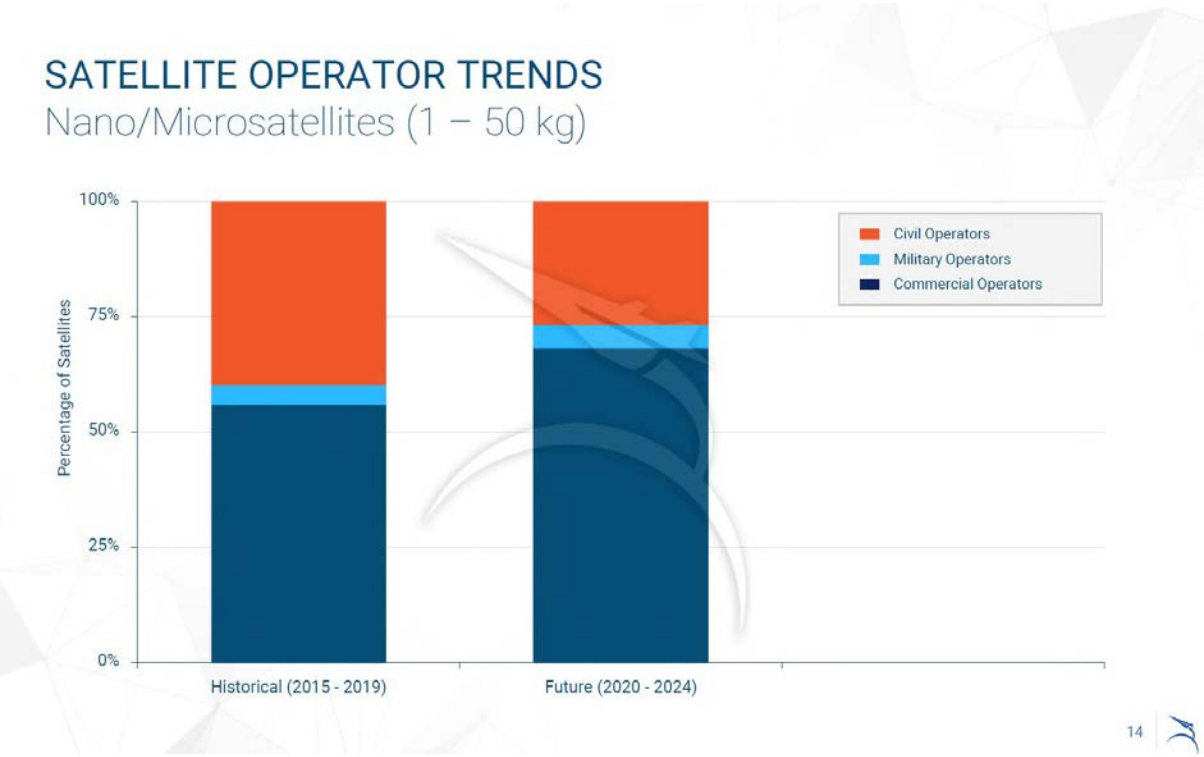

Figure 1.3: SpaceWorks 2020 data on nano and microsatellites by sector, with forecast.

2020 to retire the constellation of 5 small satellites (RapidEye, 150 kg) due to their age [14] and is now operating only nanosats, offering a constantly updated imagery service using the PlanetScope constellation of over 120 3U-CubeSats [13], the low altitude of these nanosats and their high number enables the company to offer a daily monitoring service with 3-5 m ground resolution [12]. Although the resolution is lower than state-of-the-art full size satellites (GeoEye-1 has a resolution of 0.4 m [4]) and with lower color accuracy [45], the images are more frequently updated (compared to a revisit time of 3 days for GeoEye-1) and this is more important for some applications.

Miniaturized satellites are also a convenient choice for expendable technology demonstrators due to their size and affordability: NASA sent two CubeSats (MarCO-A, MarCO-B) to Mars to test a communication system [10], BioSentinel is a 6U CubeSat to study space radiation effects on yeast [50], the ESA funded the RACE mission to demonstrate autonomous docking between to 6U CubeSats (developed by the company GomSpace) [7].

Year after year, companies are finding new commercial applications for these nanosatellites and these are growing faster in number than civil nanosatellites (research, educational) as we can see in the SpaceWorks 2020 forecast [28] (Figure 1.3).

While the industry is moving from large satellites to small form factor ones, in the nanosat

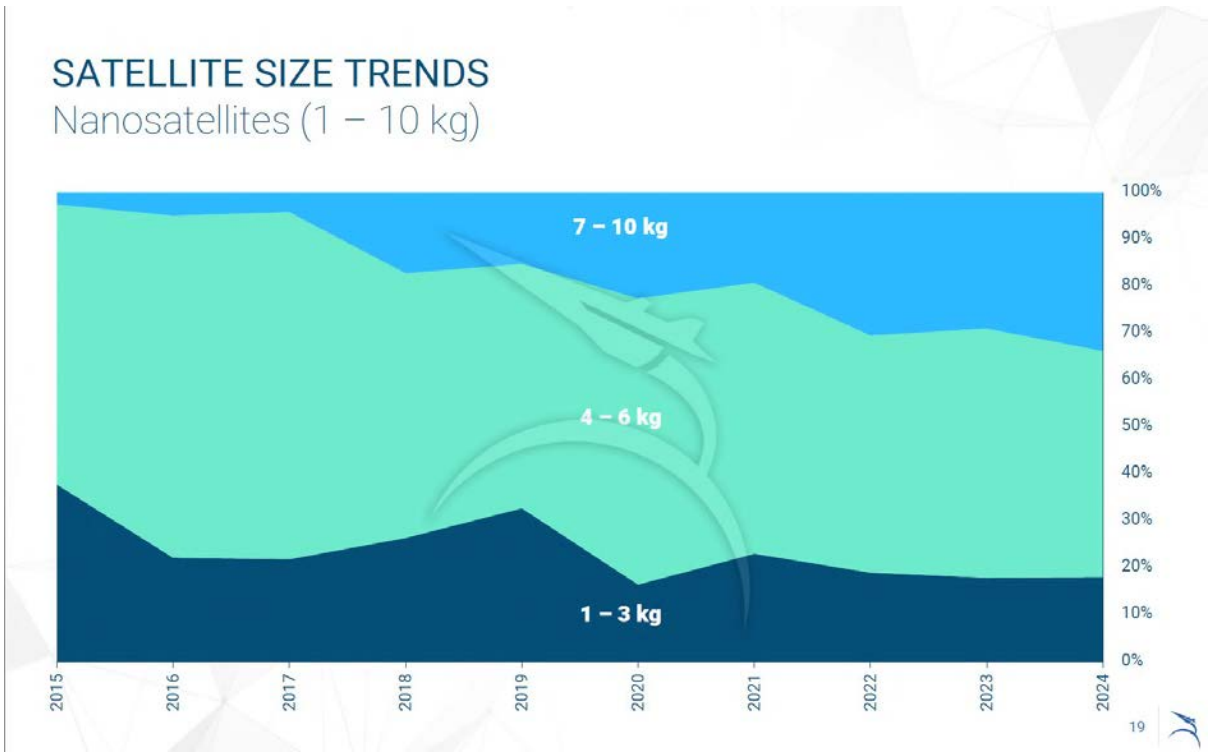

Figure 1.4: SpaceWorks 2020 data on nanosatellites evolution of weight.

category there is an ongoing shift to larger, heavier units [28] (Figure 1.4), especially in the 7-10 kg range, as these spacecrafts become more complex and mature. As we move away from the very compact 1U CubeSat to larger units, it becomes easier to integrate a propulsion subsytem into these tiny satellites that could enable orbital maneuvers, extended mission lives in low orbits, fast de-orbiting, formation flying.

Even with the advent of specialized small launchers, as of today the vast majority of nanosatellites are still launched as "piggyback" (Figure 1.5). In this scenario, a propulsion system becomes even more useful to move to the desired orbit.

In short, miniaturized propulsion solutions are necessary to keep the exponential market growth in the nanosatellites segment of recent years and there is strong interest from industries and governments alike [40]. However traditional propulsion units are difficult or simply unfit to be scaled to these sizes, so there is an intense development effort to bring to the market new propulsion units specifically designed for CubeSats and many different approaches have been proposed [38].

Europe stepped in recently, with the European Space Agency (ESA) funding 3 start-up companies to develop new compact and cost-effective launchers: Rocket Factory Augsburg, Isar Aerospace and HyImpulse Technologies.

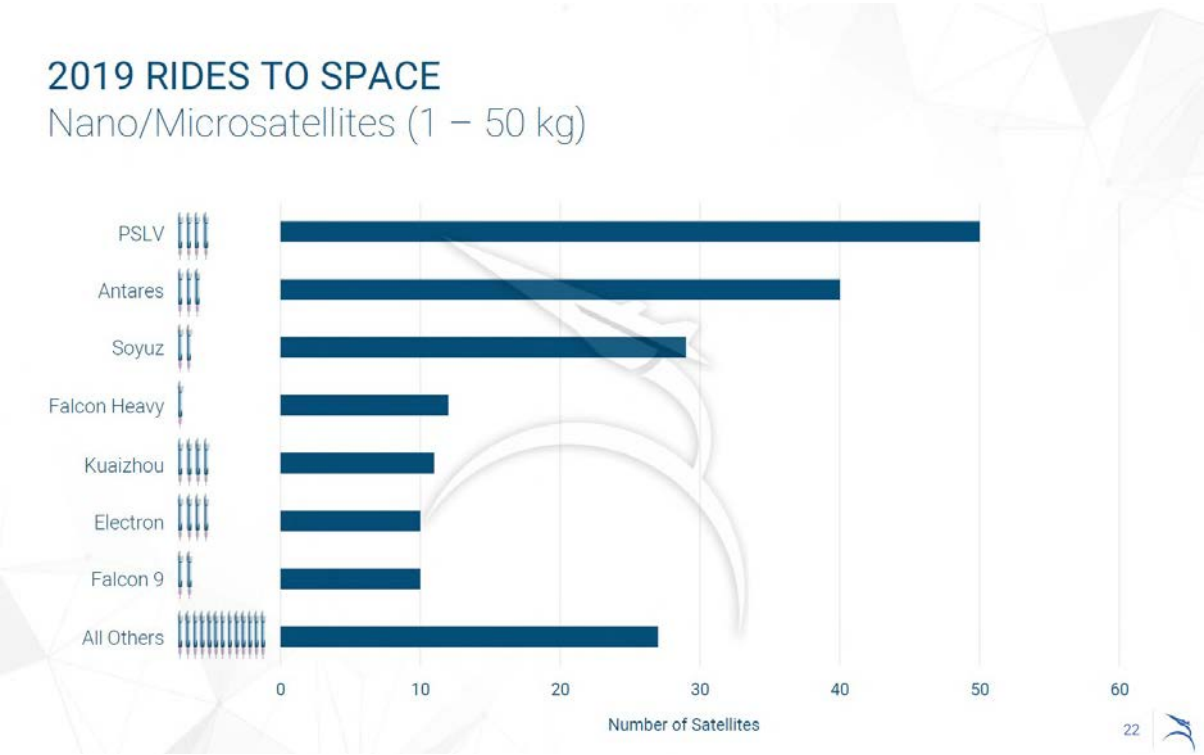

Figure 1.5: SpaceWorks 2020 data on launchers used for micro and nanosatellites in 2019.

Europe stepped in recently, with the European Space Agency (ESA) funding 3 start-up companies to develop new compact and cost-effective launchers: Rocket Factory Augsburg, Isar Aerospace and HyImpulse Technologies.

2 Elements of space propulsion

2.1 Fundamentals of rocket propulsion

All rocket propulsion is essentially based on Newton's third law of motion: for every action, there is an equal and opposite reaction. The most common propulsion system for space applications is the *chemical propulsion* [49], which uses a combustion reaction to increase the internal energy of gases that are then expanded and accelerated in a supersonic nozzle. The well known *thrust equation* (eq. 2.1) [29] defines the force that can be produced by a chemical propulsion system, as the one pictured in Figure 2.1:

$$F = \dot{m}v_e + (p_e - p_a)A_e \tag{2.1}$$

Where:

- $\dot{m}$: mass flow rate
- v_e : exhaust velocity
- p_e : exhaust pressure
- p_a : ambient pressure
- A_e : area of the exhaust section

This equation tells us there are two contributes to the thrust: the momentum of the ejected mass and the pressure difference at the exhaust section. However these two terms are not independent of each other, they are actually inversely correlated and their values are determined by the nozzle (for the same ambient pressure). It can be shown that the maximum thrust (for a given mass flow rate) occurs when the second term is null [29], i.e. the exit pressure of the propellant is the same as the ambient. This is called an *adapted nozzle* or *ideal expansion* condition and it's only valid at a given ambient pressure, which is varying with altitude, going from about 101325 Pa at sea level to almost zero in space.

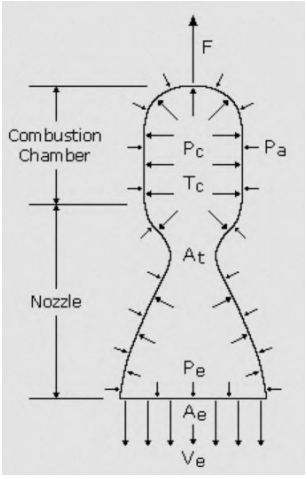

Figure 2.1: Scheme of a classic rocket motor

Equation 2.1 can be written in another form, for a more

practical use:

$$F = \dot{m}\left[v_e + \frac{A_e}{\dot{m}}(p_e - p_a)\right] = \dot{m}c = \dot{m}c^* c_F \tag{2.2}$$

If the nozzle throat is sonic, we can write

$$c^* = \frac{A_t p_c}{\dot{m}} = \frac{\sqrt{\gamma R T_c}}{\gamma\left(\frac{2}{\gamma+1}\right)^{\frac{\gamma+1}{2(\gamma-1)}}} \tag{2.3}$$

and

$$c_F = \frac{F}{A_t p_c} = \left\{\frac{2\gamma^2}{\gamma-1}\left(\frac{2}{\gamma+1}\right)^{\frac{\gamma+1}{\gamma-1}}\left[1-\left(\frac{p_e}{p_c}\right)^{\frac{\gamma-1}{\gamma}}\right]\right\}^{\frac{1}{2}} + \frac{(p_e - p_a)}{p_c}\frac{A_e}{A_t} \tag{2.4}$$

Where:

- $\gamma = c_p/c_v$: specific heat ratio
- $R = \mathcal{R}/M_m$: specific gas constant
- A_t : throat section area
- T_c : chamber total temperature
- p_c : chamber total pressure

$\frac{A_e}{A_t}$ is an important parameter called *expansion ratio* or *area ratio*, often indicated with the Greek letter ϵ [49].

c is the *effective exhaust velocity*, it is a fictional velocity (unless the nozzle is adapted) that produces the same thrust as the sum of the terms into the square brackets in Equation 2.2 multiplied for a given mass flow rate. It can also be seen as the product of *characteristic velocity* (c^*) and *coefficient of thrust* (c_F). The first one has the dimensions of a velocity, while the latter is dimensionless.

This is useful because c^* is only related to the conditions inside the combustion chamber while c_F is related to the nozzle. As γ does not usually vary much for different exhaust gases, its influence over c^* is quite limited [49]. The characteristic velocity is usually optimized by means of the ratio $\sqrt{\frac{T_c}{M_m}}$, i.e. by a high combustion temperature and a low molecular weight of the exhaust gases (check Equation 2.3 and recall that R given by the universal gas constant divided

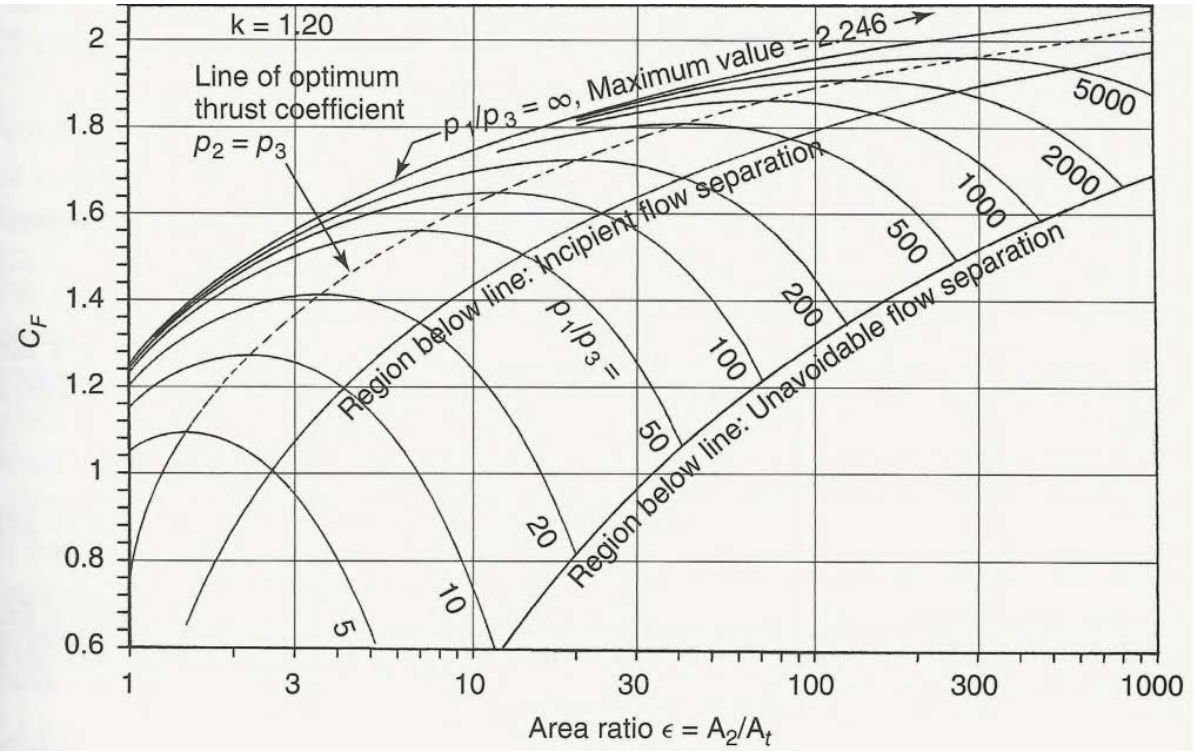

Figure 2.2: Thrust coefficient (c_F) diagram for a propellant with $\gamma = 1.2$

by the molecular mass).

c_F for a given operating altitude can be optimized with $p_e = p_a$ as already mentioned (see Figure 2.2), these pressures are controlled by the *expansion ratio* but if the latter is too high and the engine operates in atmosphere, there is a risk of generating shock-waves and flow separation (which of course are undesirable and negatively affect performance) [29]. c_F reaches an absolute maximum (for a given gas mixture) when $p_e = p_a = 0$, which means an infinite nozzle operating in vacuum, however a very large nozzle is impractical due to the weight and volume required, so a trade-off must be made [29].

As the final objective of a space propulsion system is to generate a change in velocity Δv, we should find it: now we know that thrust equals mass flow rate times the effective exhaust velocity:

$$F = \dot{m}c \tag{2.5}$$

We can rewrite the mass flow rate as the time derivative of the mass lost by the rocket:

$$\dot{m} = -\frac{dm}{dt} \tag{2.6}$$

Knowing also that $F = m\frac{dv}{dt}$ (second law of motion), Equation 2.5 becomes:

$$m\frac{dv}{dt} = -\frac{dm}{dt}c \tag{2.7}$$

and by integrating between the initial and final conditions:

$$\int_{v_i}^{v_f} dv = -c\int_{m_i}^{m_f} \frac{dm}{m} \tag{2.8}$$

we easily get:

$$\Delta v = c\ln\left(\frac{m_i}{m_f}\right) \tag{2.9}$$

which is known as the *Tsiolkovsky equation* or *ideal rocket equation* [29]. There is also the alternative form:

$$m_i = m_f e^{(\Delta v/c)} \tag{2.10}$$

It is easily apparent how important the parameter c is for propulsion: the initial mass increases exponentially with the requirement of Δv and the effective exhaust velocity is the only term that limits this growth. m_f is the mass at the end of the burn, which is a requirement of the mission.

2.2 Efficiency and performance parameters

To compare the performance of space propulsion systems it is not sufficient to look at the nominal thrust. In fact thrust does not even appear in Equation 2.10. To evaluate the performance, especially for engines operating in space, c is of great interest, but it is usually presented in the form of *specific impulse* I_{sp}:

$$I_{sp} = \frac{c}{g_0} \tag{2.11}$$

by diving by ground gravity acceleration g_0 we have a parameter with the dimensions of time (seconds) that can be used internationally. If we integrate the thrust in time we obtain another parameter called *total impulse*:

$$I = \int_{t_i}^{t_f} F dt \tag{2.12}$$

and from this we can also get a measure of how well optimized the total mass is for a given total impulse, through the parameter known as *system-specific impulse*:

$$I_{ssp} = \frac{I}{m} \tag{2.13}$$

A similar information, but restricted to the propellant, is given by the *impulse density* which is simply the specific impulse times the propellant (storage) density:

$$I_\rho = I_{sp}\rho \tag{2.14}$$

c^* is also widely used as a performance parameter, it is the main focus of research when developing a rocket engine. Nozzle technologies are well-established and they cannot increase performance (i.e. c_F) above the maximum allowed by Equation 2.4 anyway. This means the thermochemical reaction in the combustion chamber can only produce a certain *maximum exhaust velocity* or *limit exhaust velocity* [49]:

$$(v_e)_{max} = \sqrt{\frac{2\gamma R T_c}{\gamma - 1}} \propto c^* \tag{2.15}$$

This expression is proportional to c^* (compare to Equation 2.3) and they both are proportional to the speed of sound ($\sqrt{\gamma RT}$) of the gas, so maximizing the latter becomes the main scope of the research in chemical propulsion.

It must be noted that $(v_e)_{max}$ is a purely theoretical value that is impossible to achieve in a real system, this is so due to the real effects that are not accounted for in the ideal and isoentropic analysis done until this point. In fact we could write Equation 2.11 as:

$$I_{sp} = \frac{(c)_{ideal}}{g_0}\eta = \frac{(c^* c_F)_{ideal}}{g_0}\eta_{c^*}\eta_{c_F} \tag{2.16}$$

η_{c^*} is the *combustion efficiency* or *characteristic velocity efficiency*, it is the ratio of the actual change in enthalpy of the propellant to the ideal combustion change in enthalpy [49], but the latter is dependent on the assumptions used for the thermochemical evaluation (frozen equilibrium,

shifting equilibrium or chemical kinetics) [29].

η_{c_F} is the *nozzle efficiency* and it accounts for many effects such as [49]:

- *divergence of the flow*: the exit direction of the flow is usually not parallel to the engine axis.
- *boundary layer*: at the wall the fluid has zero velocity and this reduces the overall fluid momentum.
- *pressure losses*: the nozzle throat (a restriction) and the change of cross section along the nozzle introduce a pressure loss in the fluid.
- *real gas properties*: real gases have different γ and molecular mass than the ideal gas.
- *throat erosion*: the throat can be eroded by the mix of high temperatures and high flow rate in the region, a larger throat changes the chamber pressure and the expansion ratio.
- *multiphase flow*: unburnt solid particles and liquid droplets do not follow the laws of gas dynamics.

2.3 Chemical and electric propulsion

In chemical propulsion the energy that ultimately creates thrust comes from the propellant itself, through a chemical reaction. In electric propulsion systems the energy comes from something external to the propellant and it is converted into electricity at some point.

Chemical propulsion systems can be divided in 3 subcategories depending on the stored propellant state of matter:

- *liquid*: the propellant is stored in liquid form, it can be two separate liquids (bipropellant) or just one (monopropellant). While the former can achieve higher I_{sp}, the latter is simpler, generally lighter and cheaper to manufacture [29].
- *solid*: the propellant is composed of oxidizer and fuel (just like bipropellant liquid engines) and these are stored in a solid form called *grain*. Once ignited it is not throttleable and cannot be shut down.
- *hybrid*: when the oxidizer is liquid and the fuel is solid or the other way around, although the former configuration is more common and for this reason is called *classical configuration* [49].

Liquid propulsion systems are called *rocket engines*, solid ones are called *rocket motors* and for hybrid ones either term is acceptable [49].

Electrical propulsion systems are divided by how the propellant is accelerated:

- *electrothermal*: the propellant is heated and accelerated by means of a nozzle. Examples are: *resistojets* where the heating is provided through an electric resistor; *arcjets* where the heating element is an electric arc.
- *electrostatic*: the propellant is charged, forming ions (e.g. *Hall-effect thruster*) or charged droplets (e.g. *electrospray thruster*) that are accelerated by an electric field.
- *electromagnetic*: the propellant is heated to a plasma state and accelerated by an electromagnetic field. *Magnetoplasmadynamic* (MPD) and *pulsed plasma thrusters* (PPT) fall into this category.

Without diving into the details of the many different kinds of electrical thrusters, we can make a couple of general observations when comparing chemical and electrical propulsion: thrust produced is very low for electrical thrusters (Figure 2.4), making them unsuitable to propel launchers and make fast maneuvers in space, however the propellant is used extremely efficiently (high specific impulse), making these systems attractive for space uses like station keeping or deep space travel [49]. One of the reasons of the low thrust is found in Figure 2.3: power requirements for electrical thrusters are very high. While chemical engines only need to power auxiliary components like valves, thrust vectoring, control electronics, electrical thrusters cannot count on the dense energy storage of chemical bonds, they need a spacecraft capable of extracting/storing a high amount of electrical power and this, of course, comes at the cost of additional weight (batteries and power delivery system) and size (solar panels).

In Figure 2.5 there is a summary of the main properties of the different kinds of space propulsion systems. A common technology is the cold gas thruster, which is extremely simple (a pressurized gas is let out of a convergent-divergent nozzle, without heating), reliable and safe. The simplicity however comes with a low I_{sp}, high tank pressures and a thrust output that decreases through use. Monopropellant liquid engines have somewhat low I_{sp} but require less parts and complexity than bipropellant ones, which are more efficient. In fact, bipropellant engines feature the highest I_{sp} of the chemical group, solid motors can provide high thrust but with a lower I_{sp}. Hybrid engines, being a mix of the two technologies, has performances in between, with the benefits of being throattleable, restartable and safer compared to solid motors [49].

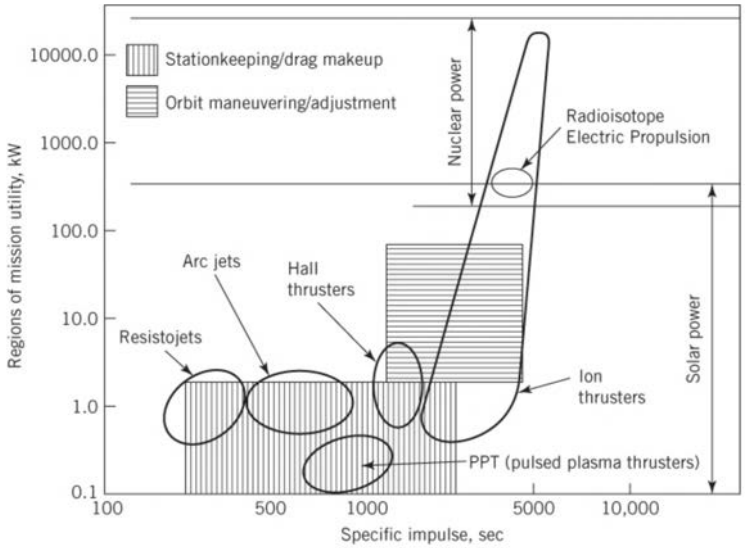

Figure 2.3: Comparison of typical power requirement and I_{sp} of different chemical and electrical propulsion systems. Reproduced from [49].

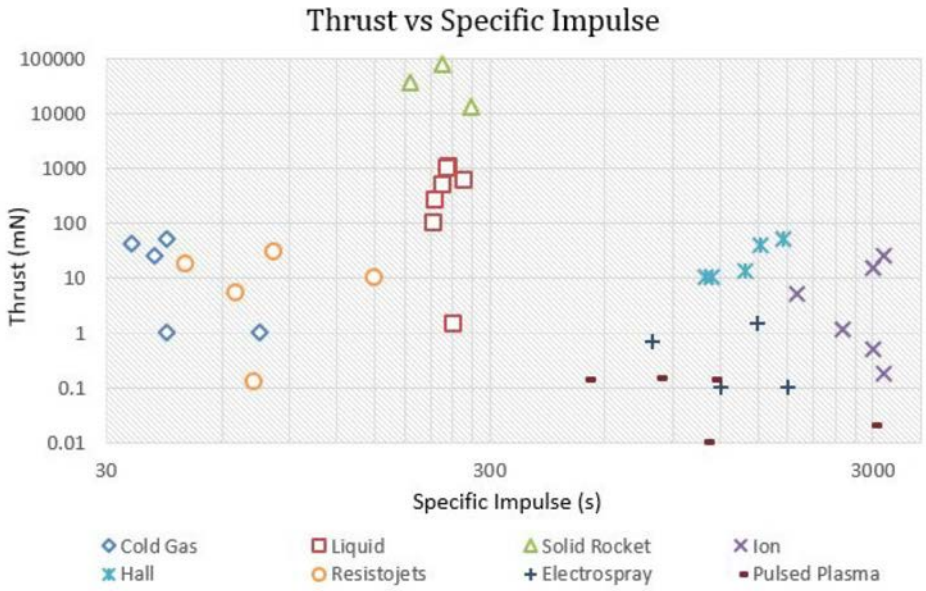

Figure 2.4: Comparison of typical thrust and I_{sp} of different chemical and electrical propulsion systems. Reproduced from [51].

Technology	I_{sp} (s)	Thrust (N)	Advantages	Disadvantages
Cold Gas		0.1–50	• simplicity • safe • low contamination	• low specific impulse
N_2	60			
H_2	250			
Chemical		0.1–12,000,000	• high thrust • heritage	• moderate performance • combustion complications • safety concerns
Liquid				
Monopropellant	140–235			
Bipropellant	320–460			
Solid	260–300			
Hybrid	290–350			
Nuclear		up to 12,000,000	• high specific impulse	• unproven • politically unattractive • expensive • low thrust/weight
Solid core	800–1100			
Liquid core	3000			
Gas core	6000			
Electric		0.0001–20	• very high specific impulse	• high system mass • low thrust levels • limited heritage
Electrothermal	500–1000			
Electromagnetic	1000–7000			
Electrostatic	2000–10,000			

Figure 2.5: Summary of the properties of the different space propulsion technologies. Reproduced from [29]

2.4 The challenges of miniaturized CubeSat propulsion

The CubeSat standard, detailed in the document *CubeSat Design Specification* (CDS) by the California Polytechnic State University, was originally created to enable very low cost launches for educational purposes. As such, one of the main concerns was that the CubeSat would not pose any risk or interference to the primary payload of the launch and many limitations on the CDS made the implementation of propulsion systems difficult [38] and thus hampering the introduction of CubeSats with propulsion in space. Very few CubeSats have flown with propulsion systems and many of those who did, carried safe low I_{sp} cold gas thrusters [44].

As more more specialized missions are being developed for these nanosats, some concessions are being made: for example in the draft of CDS Revision 14 (the most recent at the day of writing) [34], the prohibition of pyrotechnics has been lifted, opening the way to the use of solid motors and ignition systems, the limit of 100 Wh of total stored chemical energy has been removed as well. The CDS design rules are not immovable restrictions, but obtaining a waiver to circumvent the requirements is often difficult and prohibitively expensive [38].

The latest revision of CDS mainly asks propulsion systems to be in accordance to the *Air Force Space Command Range Safety Manual (91-710) volume 3* and to feature at least 3 inhibits to activation. This would not be an issue in full size spacerafts, but in nanosatellites every bit of volume is precious. As a matter of fact, I_{sp} cannot be used alone to evaluate CubeSat propulsion systems, impulse density or system specific impulse need to be always taken into consideration [38]. Valves are one key component in liquid engines that does not scale well in size nor in energy consumption, but there has been some progress with Micro-ElectroMechanical Systems (MEMS) technology that enables small and efficient valves with precise regulation of tiny flow rates [44].

Monopropellant liquid engines are relatively simple and reliable, but most of them were historically based on hydrazine which is being slowly phased out in all satellites due to its extreme toxicity [3]. On CubeSats hydrazine is hardly acceptable also due to the risk of autocombustion [38]. The best monopropellant alternatives at the moment are hydroxylammonium nitrate (HAN) and ammonium dinitramide (AND) but they require heating to 250°C to achieve a reliable ignition, which means a significant amount of electrical power from a CubeSat [38].

Bipropellant liquid engines need twice the piping and valves of monopropellant ones, but their higher I_{sp} can make up for the volume lost by those. The added complexity means very few systems of this kind exist today for CubeSats, but two examples are the *Hydros-C* from Tethers Unlimited Inc. [15] and the *CubeSat Propulsion Module* from Dawn Aerospace [9]. The former

uses water dissociated by electrolysis and can produce 1.2 N of thrust with an I_{sp} of 310 s, consuming 25 W of electrical power, the latter is a nitrous oxide (N2O) + propene (C3H6) engine, producing 0.33 N to 1 N of thrust depending on tank temperature with an I_{sp} in excess of 285 s.

3 Development of a new bipropellant liquid engine

3.1 Challenges specific to liquid bipropellant micropropulsion

3.1.1 Piping and tanks

As previously mentioned, two separate propellants means two tanks are needed, and twice the piping, seals and valves as well. Additive manufacturing could be used to help reduce the number of connections needed, thus reducing the possible points of failure and at the same time optimizing the little space available inside the satellite.

3.1.2 Pressurization

All liquid engines need a system to force the propellant from the tank(s) to the combustion chamber where the reaction happens. Classical bipropellant engines usually rely on gas-pressurization or turbopumps placed in a variety of different schemes (Figure 3.1) [29]. Self-pressurization (i.e. by means of the vapor pressure of the propellant itself) is advantageous in miniaturized liquid propulsion because it is more volume-efficient and it does not require additional parts and costs. This poses some restrictions in the choice of the propellants though: the vapour pressure must be high enough to guarantee a stable injection flow into the combustion chamber but not so high that it requires thick tank walls and massive valves. Although there is no explicit upper limit on the pressure allowed on CubeSats in the CDS [34], the higher the pressures involved the riskier the nanosat will be deemed, making it difficult to be accepted onto the launcher [44].

3.1.3 Injection and mixing

An efficient atomization and a homogeneous mixing of oxidizer and fuel are necessary to reach the maximum combustion efficiency. There are many injection designs developed over the years for liquid rocket engines but most of them rely on a pattern of many (dozens or hundreds [29]) small injectors arranged over an *injector plate* (Figure 3.2). Since the manufacturing accuracy for micropropulsion and traditional rocketry is virtually the same, it is simply impossible to fit that many injectors on an small scale engine of few centimeters in diameter. So it is still required to reach a uniform mixing but it needs to be done with just a few injecting elements.

3.1.4 Ignition

Traditional ignition strategies usually involve hypergolic mixtures, pyrotechnics or spark plugs [30]. The first one poses issues of both safety and toxicity, the last two are still a safety concern

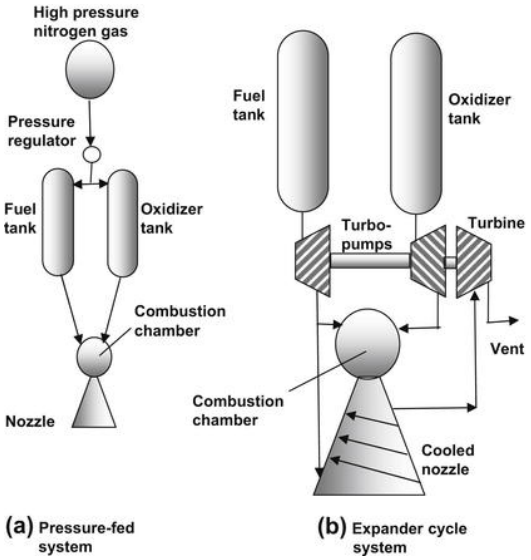

Figure 3.1: Gas pressurization and expander cycle pressurization

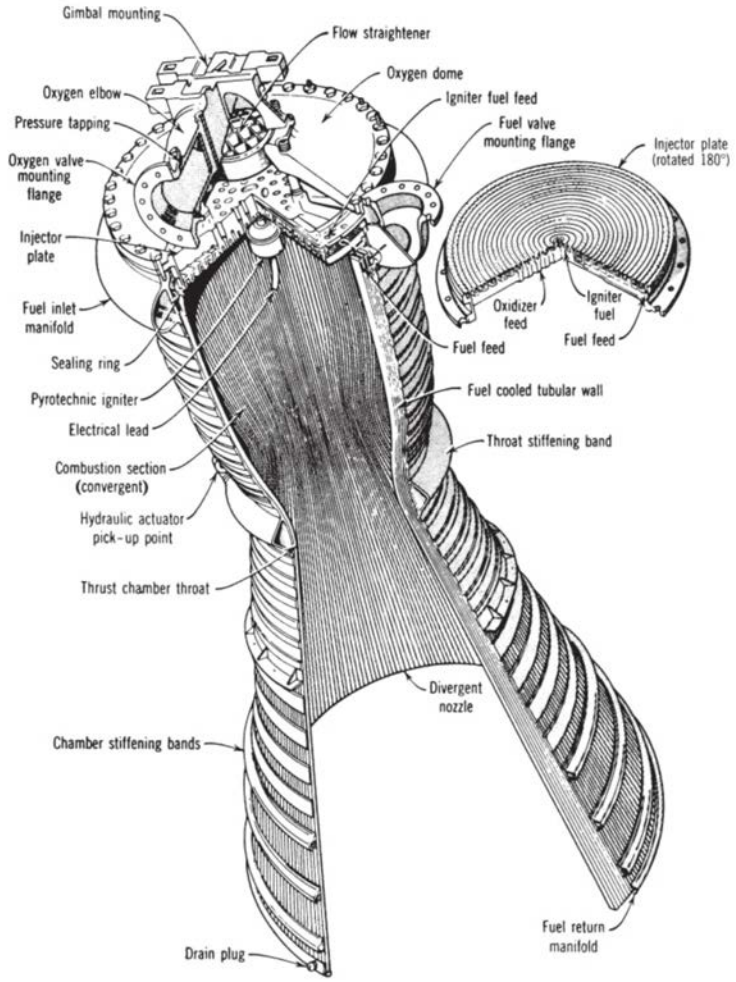

Figure 3.2: Cutout of a liquid bipropellant engine. Reproduced from [49].

for CubeSats (spark plugs because they need a high voltage circuit), although not as troubling as the first one. Pyrotechnics also have the disadvantage to be single use devices.

3.1.5 Thermal loads

In a liquid rocket engine the gases reach very high temperatures to improve the $c*$ parameter, especially in bipropellant engines these temperatures often exceed the melting point of the thrust chamber materials [49]. Heat is transferred from the hot gas to the chamber walls through radiation and convection, it is possible to operate the engine for a very short amount of time using the walls as a heat sink, but active cooling is necessary for continuous operation.

Radiation from the gas to the chamber walls follows the Stefan-Boltzmann law:

$$dq = \sigma \epsilon T^4 dS \tag{3.1}$$

where dq is the infinitesimal heat flux radiated from the surface element dS.

Convection (per surface unit) can be described by the Newton linear approximation:

$$q = h_c(T_g - T_w) \tag{3.2}$$

where h_c is the *convective heat transfer coefficient*, T_g is the local free stream gas temperature and T_w is the temperature of the wall. h_c depends on the fluid properties: thermal conductivity k, constant pressure specific heat c_p, dynamic viscosity μ and density ρ. These properties have to be evaluated at a reference *film temperature* T_f (somewhere in between the gas and the wall temperature) [27]. h_c can be written as a function of the Reynolds, Prandtl and Stanton numbers of the fluid:

$$h_c = f(Re, Pr, St) \tag{3.3}$$

or equivalently of its Reynolds, Prandtl and Nusselt numbers:

$$h_c = f(Re, Pr, Nu) \tag{3.4}$$

None of the fluid properties described above scale with the dimensions of the engine and the thermal load (per unit area) on the walls of a small engine is approximately the same as a full size one, which makes engine cooling a difficult task because the $surface/volume$ ratio is unfavourable: there is more surface to be cooled for the same unit of internal volume (which

is related to the thrust produced, for the same chamber pressure). Structural integrity at high temperatures is not the only concern for miniaturized engines: losing heat to the chamber walls means losing energy that would otherwise generate thrust, so the design should focus primarily on minimizing the heat transfer rather than just on keeping the temperature of the walls low [30].

3.2 Requirements of this new engine

By taking into account the market data that indicates a continuously growing focus on nanosatellites (1-10 kg) [Chapter 2] and the characteristics of the existing bipropellant engines, it has been set for this work that a new and competitive chemical propulsion system should have the following features:

- 1 N nominal thrust
- safe and storable propellants
- 90% HTP as oxidizer
- I_{sp} >270 s
- additively manufactured combustion chamber
- $\eta_{c*} > 90\%$
- multiple restarts
- capable of continuous operation
- operating temperature between -10 °C and 50 °C
- be able to be tested at 1 atm (i.e. without a vacuum test chamber)

Also, the impulse density should be prioritized in place of the specific impulse, since the volume of nanosatellites is a more stringent constraint than their weight.

HTP 90% (High-Test Peroxide) has been selected as the oxidizer due to the long experience and know-how gained with it by the people at the University of Padua and its other desirable features such as:

- high density: $1390 kg/m^3$ @20°C
- can act as a monopropellant (catalytic decomposition)
- allows an "hypergolic" ignition with many fuels due to its high decomposition temperature: 1020 K

- relatively safe due to its very low vapour pressure: 5 mm Hg @30°C
- stable if stored correctly
- liquid under standard pressure from -10 °C to 140 °C
- obtainable via distillation of lower grade hydrogen peroxide

3.3 Proposed fuels

This work has focused on light hydrocarbons with moderate vapour pressures in the operational temperature range, this allows a self-pressurizing system with a nearly constant flow rate during the firing of the engine (provided the heat flux due to vaporization is roughly equal to the heat conducted through the tank walls). This approach would also save the volume in the tanks that would be necessary to store a pressurizing gas. However, the selection of the ideal fuel to be paired with HTP is outside the scope of this thesis, but suggestions will hereby be made: propane, propene (also known as propylene), propyne (also known as methylacetylene).

Table 3.1: Fuel candidates

Hydrocarbon	**Vapour pressure**			**Density (liquid)**
	@-10°C [bar]	@25°C [bar]	@50°C [bar]	@50°C [kg/m^3]
Propane (C3H8)	3.45	9.52	17.14	449
Propene (C3H6)	4.29	11.58	20.58	456
Propyne (C3H4)	2.65	5.82	11.35	570

In Table 3.1 are summarized some relevant physical properties of these fuels, taken from the NIST Chemistry WebBook site [19]. Density is listed for the temperature of 50 °C since it is the condition that dictates the minimum volume for tanks.

Using the thermochemical propellant evaluation tool CPROPEP, which is the updated version of the FORTRAN program developed originally by the Martin Marietta Corporation (now Lockheed Martin) [36], it was possible to generate some performance comparison plots between the 3 fuels, setting a frozen flow for all simulations:

- Fig. 3.3 shows the ideal impulse density for each oxidizer/fuel mixture ratio (O/F), this is evaluated as:

$$I_\rho = I_{sp}\rho = \frac{c^* c_F \rho}{g_0} \tag{3.5}$$

  where the density ρ is the weighted average of the densities of fuel and oxidizer, so it is a function of O/F. c_F is calculated from Eq. 2.4 assuming an expansion ratio of 100.

- Fig. 3.4 compares the specific impulse, which gives a measure of how efficiently the propellant mass is used to generate thrust.
- Fig. 3.5 compares the flame temperature inside an adiabatic chamber, this gives an idea of how difficult would be to cool the combustion chamber to preserve it from damage.

We can see the three hydrocarbons perform quite similarly at around O/F=7. The choice should be a trade-off between the I_{sp}, I_ρ and flame temperature, there is no universally best choice. This work focuses on developing a good fluid-dynamic design that is additively manufacturable, all the CFD simulations will be based on the HTP/propyne pair, since it maximizes the impulse density (at O/F=6.5), but the fluidic design can be applied basically to any other fuel/oxidizer pair with a similar O/F and gas/gas injection. Compatibility of propyne with metals and the effectiveness of stabilizing additives should be investigated, since it is prone to explosive decomposition if in contact with copper alloys and oxidizers [20].

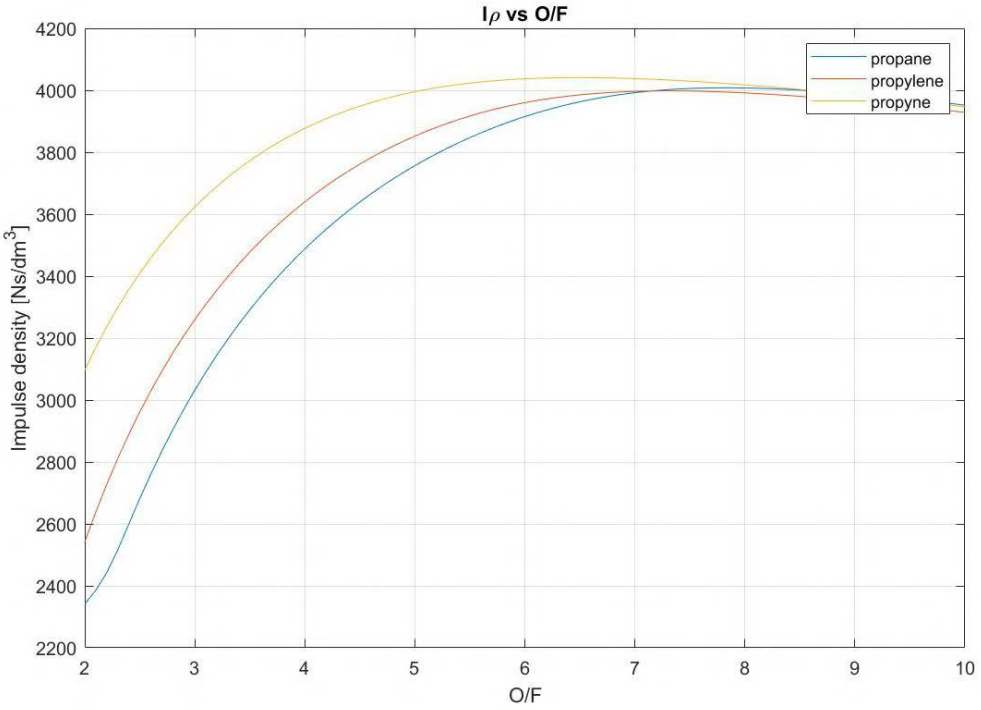

Figure 3.3: Impulse density comparison for 1 liter of total tanks volume.

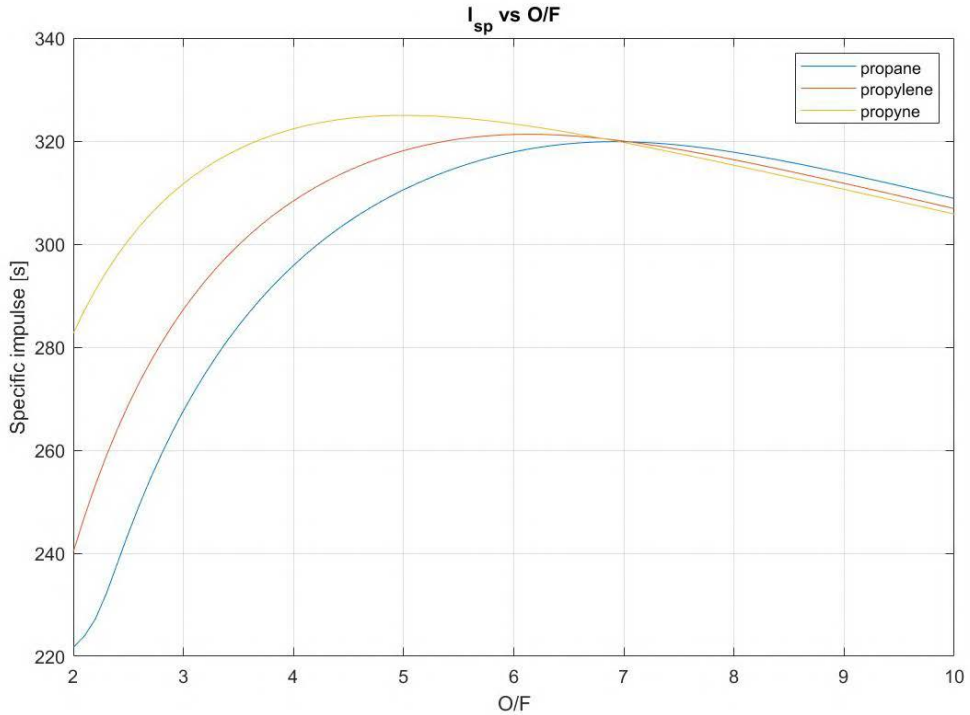

Figure 3.4: Specific impulse comparison.

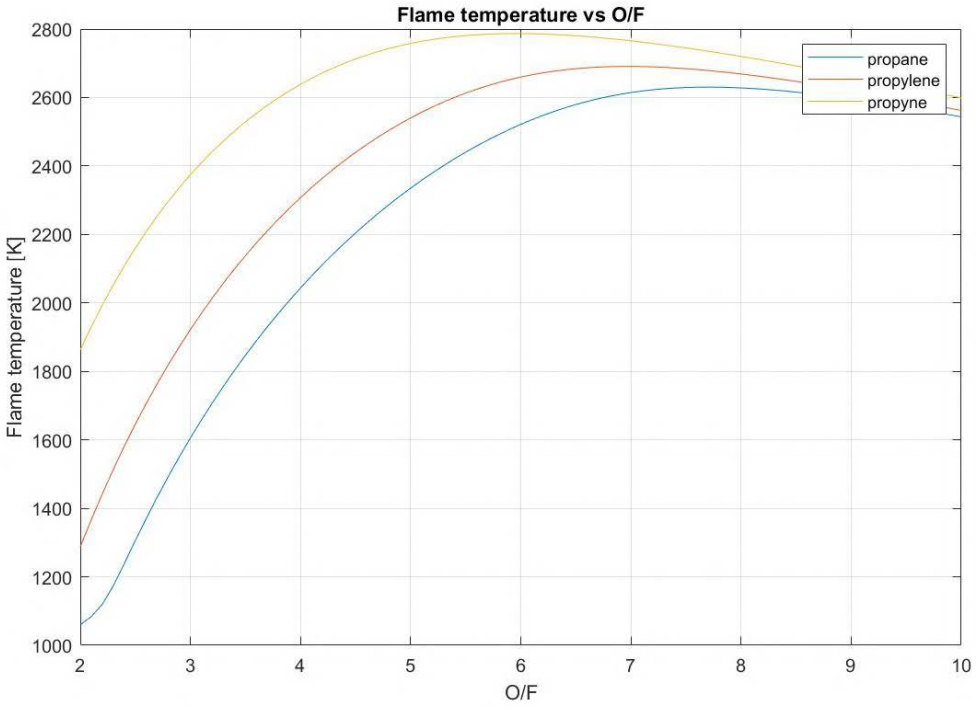

Figure 3.5: Flame temperature comparison.

3.4 Nozzle

An expansion ratio $\epsilon = 100$ is used for the nozzle. It is clear we should take advantage of additive manufacturing and opt for the more efficient and shorter bell nozzle design. The conical nozzle has only the advantage of being easier to manufacture through classical machining. The exact science to generate the optimum bell contour employs the *method of characteristics* and it is not trivial [30]. The parabolic approximation by G.V.R. Rao [46] is employed here instead to generate an 80% bell nozzle (80% of a 15° conical nozzle equivalent).

The convergent section is a truncated cone with a 60° half-angle, but this can be modified to 45° or less to comply with additive manufacturing restrictions without an effect on performance. The resulting nozzle is pictured in Fig. 3.6.

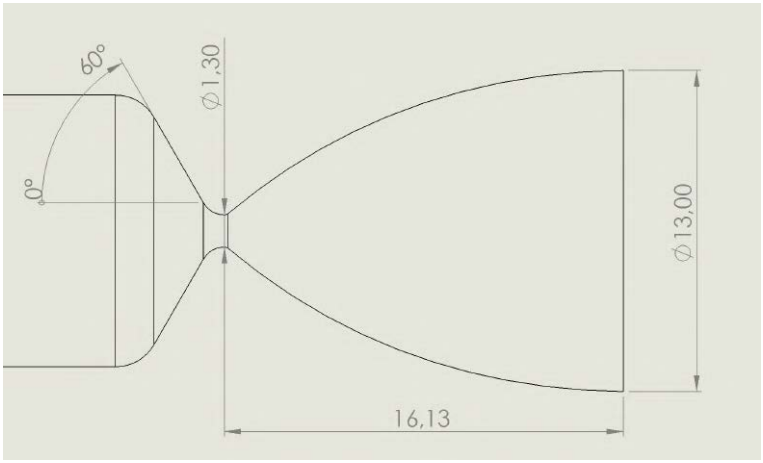

Figure 3.6: Nozzle design used in the simulations.

3.5 Combustion chamber design

3.5.1 Pressure

Nominal operation pressure is set to 4 bar, calculated as 70% of propyne vapour pressure at 25°C (5.82 bar), thus allowing a 30% pressure drop through the feed system.

3.5.2 Chamber dimensions

In order to allow for a complete combustion of the reactants, these require to be efficiently mixed and to have enough time to reach chemical equilibrium before they are expelled. The *residence time* is the average time the propellants stay inside the chamber from injection to the throat, however the *characteristic length* is a much more practical parameter from an engineering standpoint [30], defined simply as the ratio of chamber volume and throat area:

$$L^* = \frac{V_c}{A_t} \tag{3.6}$$

c^* is influenced by L*: in an adiabatic chamber the higher the L*, the better the c^* value, up to an asymptotic maximum [30]. For an estimate of the L* required, experimental data is available from past engine designs, as in Fig. 3.7. We can see propellant pairs with a gaseous fuel injection generally require $L^* = 0.5 - 0.7m$, thus a cautious value of $L^* = 0.8m$ will be used in this work.

Having L^*, we need the ratio of physical length to diameter for the chamber and the throat area. The former is a choice left to the designer, the latter comes from Eq. 3.7 and Eq. 3.8.

Propellant Combination	Combustion Chamber Characteristic Length (L*), in.
Chlorine trifluoride/hydrazine-base fuel	20-35
Liquid fluorine/hydrazine	24-28
Liquid flourine/liquid hydrogen (GH_2 injection)	22-26
Liquid fluorine/liquid hydrogen (LH_2 injection)	25-30
Hydrogen peroxide/RP-1 (including catalyst bed)	60-70
Nitric acid/hydrazine-base fuel	30-35
Nitrogen tetroxide/hydrazine-base fuel	30-35
Liquid oxygen/ammonia	30-40
Liquid oxygen/liquid hydrogen (GH_2 injection)	22-28
Liquid oxygen/liquid hydrogen (LH_2 injection)	30-40
Liquid oxygen/RP-1	40-50

Figure 3.7: Typical characteristic length values. Reproduced from [30].

$$\dot{m} = \frac{F}{c^* c_F} \tag{3.7}$$

$$A_t = \frac{\dot{m} c^*}{p_c} \tag{3.8}$$

In an attempt to minimize the surface-to-volume ratio that impacts the thermal flux at the engine walls, the length/diameter ratio has been set equal to 1 in the non-swirling designs (minimum surface-to-volume for a cylinder). In the swirling designs the hottest zone is always the center of the engine (along the symmetry axis), while the side walls are covered by the "cold" injection of one of the propellants. Therefore in swirling designs the length/diameter ratio has been set to 1.5, in order to generate smaller bases and a slightly longer cylinder.

3.5.3 Manufacturing constraints

In order to ensure the manufacturability through laser melting technologies, a lower dimensional limit of 0.5 mm has been set for holes and gaps. Walls will have a minimum thickness of 0.8mm. Where very thin edges were present in aerodynamically relevant regions, a 0.15 mm fillet radius has been applied to better represent what the future manufactured part would look like with limited printing definition. Almost-closed volumes are avoided where possible, since unused metal powder needs to be removed from the inside.

3.6 Simulated system summary and expected performance

To summarize, the system being numerically simulated in this work has the following theoretical features:

- fuel = propyne
- oxidizer = HTP 90%
- $c^* = 1599\ m/s$
- $c_F = 1.972$
- $p_c = 4\ bar$
- $O/F = 6.5$
- $T_c = 2780\ K$
- throat diameter = 1.3 mm
- $\epsilon = 100$
- $L^* = 0.8\ m$

Before any simulation was made, a combustion efficiency of 0.92 and a nozzle efficiency of 0.95 were assumed, leading to an expected I_{sp} of about 281 s.

4 CFD simulations

4.1 Brief overview of the theory

4.1.1 RANS equations

The well-known Navier-Stokes equations, using Einstein's notation, are written (no external forces):

$$\frac{\partial \rho}{\partial t} + \frac{\partial (\rho u_i)}{\partial x_i} = 0 \tag{4.1}$$

$$\frac{\partial (\rho u_i)}{\partial t} + \frac{\partial (\rho u_i u_j)}{\partial x_j} = -\frac{\partial p}{\partial x_i} + \frac{\partial \tau_{ij}}{\partial x_j} \tag{4.2}$$

$$\frac{\partial (\rho E)}{\partial t} + \frac{\partial [u_i(\rho E + p)]}{\partial x_i} = \frac{\partial (\tau_{ij} u_j)}{\partial x_i} - \frac{\partial q_i}{\partial x_i} \tag{4.3}$$

Where $E = e + \frac{1}{2}(u_i u_i)$ is the total energy, q_i is the thermal flux and τ_{ij} is the viscous stress tensor, defined as:

$$\tau_{ij} = \mu \left(\frac{\partial u_i}{\partial x_j} + \frac{\partial u_j}{\partial x_i} - \frac{2}{3} \frac{\partial u_k}{\partial x_k} \right) \tag{4.4}$$

These equations express respectively the conservation of mass (Eq. 4.1), momentum (Eq. 4.2) and energy (Eq. 4.3) for a Newtonian fluid.

The direct numerical solution of these differential equations for many applications requires an impractical amount of resources (time, computational power). A more affordable approach is to apply an *ensemble average* to the equations. By making use of the *Reynolds decomposition*, every term can be written as the sum of its mean $\bar{u_i}$ and its fluctuation u_i' [43]:

$$u_i = \bar{u_i} + u_i' \tag{4.5}$$

Therefore we obtain the Reynolds-averaged Navier-Stokes (RANS) equations (the energy equation is left out for simplicity):

$$\frac{\partial \bar{\rho}}{\partial t} + \frac{\partial(\bar{\rho}\bar{u_i})}{\partial x_i} = 0 \tag{4.6}$$

$$\frac{\partial(\bar{\rho}\bar{u_i})}{\partial t} + \frac{\partial(\bar{\rho}\bar{u_i}\bar{u_j})}{\partial x_j} = -\frac{\partial \bar{p}}{\partial x_i} + \frac{\partial \bar{\tau_{ij}} - \bar{\rho}\overline{u_i' u_j'}}{\partial x_j} \tag{4.7}$$

Although the equations are very similar, by using averaged quantities we have a stationary solution and there is no need to solve the finest vortices (eddies) in the flow field, saving a massive amount of computational power and memory. However the term $\bar{\rho}\overline{u_i' u_j'}$ is new and it makes the set of equations unsolvable: trying to find an analytic equation for it only results in other new averaged unknown terms over and over [43]. Therefore this term, called *Reynolds stress* needs to be modeled to close the numerical problem and this modeling is the very reason RANS simulations need to be validated with experimental measurements for reliability.

4.1.2 Eddy viscosity models

There is a class of models widely used for the Reynolds stress called the *eddy viscosity turbulence models*. The basic assumption is that turbulence acts as an additional viscosity and it is proportional to the mean deformation tensor [43].

With this assumption the averaged momentum equation becomes:

$$\frac{\partial(\bar{\rho}\bar{u_i})}{\partial t} + \frac{\partial(\bar{\rho}\bar{u_i}\bar{u_j})}{\partial x_j} = -\frac{\partial \bar{p}}{\partial x_i} + \frac{\partial\left[\mu_{eff}\left(\frac{\partial \bar{u_i}}{\partial x_j} + \frac{\partial \bar{u_j}}{\partial x_i} - \frac{2}{3}\frac{\partial \bar{u_k}}{\partial x_k}\right)\right]}{\partial x_j} \tag{4.8}$$

where μ_{eff} is the *effective viscosity*, which is the sum of the fluid viscosity and the turbulent viscosity μ_T:

$$\mu_{eff} = \mu + \mu_T \tag{4.9}$$

The model used for all the simulations in this work is the $k-\epsilon$, which provided results in good agreement with experimental data when applied to a hybrid rocket motor at the University of Padua [23]. A detailed overview of this and other eddy viscosity models is definitely beyond the scope of this text. More information is available in textbooks such as Pope [43].

4.2 Main injection designs investigated

Based on the preliminary results obtained in previous student projects, it was decided to investigate 3 "families" of injection designs that could potentially provide the low gas temperatures at the wall we need for this micro-thruster:

- **coaxial injection**: this has been called the *C series*, it features an annular injection of oxidizer, fuel is injected inside the surface delimited by the annulus.
- **swirling injection of oxidizer**: this was called the *SO series*, the injection of oxidizer is (predominantly) tangential from the side wall. The angular momentum should maintain a layer of cold oxidizer there, confining the combustion at the center.
- **swirling injection of fuel**: this was called the *SF series*, the same principle as above applies, although it must be noted the fuel mass flow rate is much smaller than the one of the oxidizer.

4.3 Swirl number

In order to quantify the degree of swirl in a fluid flow, Chigier and Beer [26] proposed the use of a scalar called "swirl number", later simplified by Sheen et al. [48] (eliminating a small contribution due to pressure) in the following form:

$$S_N = \frac{G_\theta}{RG_z} = \frac{\int_0^R u_z u_\theta r^2 \, dr}{R \int_0^R u_z^2 r \, dr} \tag{4.10}$$

Basically this swirl number is defined as the ratio of the axial flux of tangential momentum G_θ to the axial flux of axial momentum G_z.

Swirling motion helps with mixing of the reactants, however in a rocket engine excessive swirl creates a pressure gradient: due to the centripetal acceleration, the rotation creates an additional contribute of pressure near the wall. The 3-dimensional flow makes the effective throat area smaller than the geometric one, increasing the average chamber pressure compared to the predictions of uni-dimensional gas dynamics equations. Since the swirling motion also causes an increase of mixing and combustion efficiency, the sole contribution of 3-dimensional flow to the pressure is not straight-forward to quantify [25].

The practical method to determine combustion efficiency in a rocket engine (and in this work) is by measuring the actual chamber pressure p_c and comparing it to the theoretical one.

$$\eta_{c^*} = \frac{[p_c]_{measured}}{[p_c]_{theoretical}} \tag{4.11}$$

The pressure gradient associated with swirling flow makes this measurement difficult, especially in real world tests where the pressure tap can only be placed on the wall. Furthermore the residual tangential motion of the expelled fluid produces a torque on the spacecraft that could become non-negligible at very high swirl numbers.

For all these reasons, it was set a quite conservative **maximum swirl number of 0.5** for this new engine. In order to get one *a priori* estimate of the strength of the swirl for every design before simulation, a geometric swirl number was used, which is an approximation of the integral formulation and it only needs a few known parameters:

$$S_{Ngeom} = \frac{v_\theta}{v_z} \tag{4.12}$$

Where v_θ is the tangential velocity at the outer radius, v_z is the average axial velocity in the chamber. If only one of the propellants (or portion of it) is tangentially injected v_θ can be estimated as:

$$v_\theta \approx \frac{\dot{m}_{tangent}}{\dot{m}_{axial} + \dot{m}_{tangent}} v_{tangent} \tag{4.13}$$

Where "tangent" refers to the tangentially injected propellant (or portion of it).

4.4 Combustion thermochemistry

The fuel is considered to be extracted in its vapour form from the tank, this allows us to circumvent the issues with critical liquid flow: cavitation, two-phase flow, rapid changes of composition in response to varying pressure. Therefore the propellants are ready to combust when they encounter, being both already in the gas phase. The chemical reaction between the decomposed HTP 90% and propyne (C3H4) has been determined with the following procedure:

1. Calculation of the stoichiometric reaction between H2O2 and C3H4:

   $8\,H_2O_2 + C_3H_4 \longrightarrow 10\,H_2O + 3\,CO_2$

   Therefore we have a molar O/F = 8 for the H2O2/C3H4 reaction. It corresponds to a mass O/F = 6.792. By using HTP 90%, which density is 95.3% the density of pure H2O2, the

stoichiometric mass O/F ratio is 7.13.

2. Calculation of the more realistic chemical reaction using O/F = 7.13 and HTP 90% + C3H4 in CPROPEP at 4 bar chamber pressure. An adiabatic equilibrium temperature of 2760 K is obtained, along with all the product species. To accelerate the simulations in ANSYS CFX, just the 4 most abundant species (in terms of molar fraction) are selected from the combustion products:

   - CO
   - CO_2
   - H_2O
   - H_2

   These species together represent over 95% of the reaction products. Since the actual chemical reaction is not the focus of this work (nor the choice of fuel), this approximation seems very reasonable to take.

3. Calculation of HTP 90% decomposition products: 57.7% (mass) H2O + 42.3% O2.

4. Re-balancing of the chemical reaction from the first step with realistic products, decomposed HTP 90% as a reactant. By transferring the H2O from the left side to the right, we get the actual reaction to be used inside ANSYS CFX:

   $22\,O_2 + 7\,C_3H_4 \longrightarrow 9\,H_2O + 5\,H_2 + 14\,CO_2 + 7\,CO$

The eddy dissipation model is used for combustion, this model simple but effective: it has been used successfully in previous works at the University of Padua [23].

The chemical reaction is assumed to be immediate when the reactants mix at the molecular level, therefore this model has a reaction rate proportional to the dissipation ϵ:

$$rate = \frac{\epsilon}{k} \tag{4.14}$$

This model can be applied successfully where the chemical kinetics are very fast compared to the mixing time, which is the case of many industrial combustion problems [31].

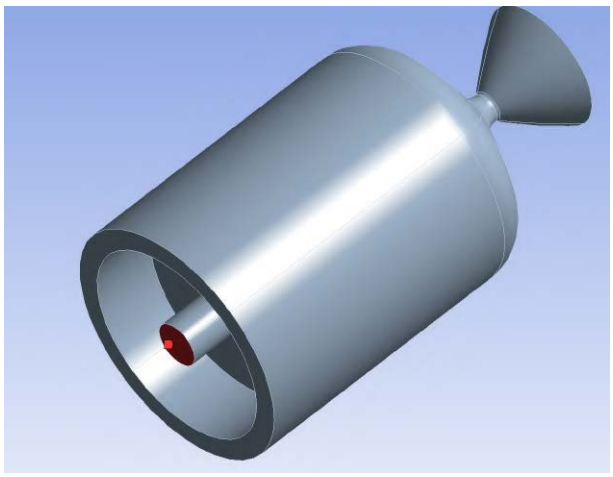

Figure 4.1: Configuration C1.1.

4.5 Mesh

4.5.1 General meshing approach

To perform the calculations the fluid domain must be divided in discrete elements. In this work an **unstructured mesh with tetrahedrons cells** has been applied to all configurations, **high resolution differencing schemes** have been set for advection and turbulence. **Wall functions** have been used to represent the boundary layer, saving computational cost. Another time-saving measure adopted was to cut the nozzle at around $\epsilon = 19$ to reduce the mesh elements number by over a third. The physics of nozzle flow are a well-known subject in literature and not of interest for this investigation, so cutting most of it had no consequence.

To be sure the number of mesh elements is sufficiently high, an initial *mesh sensitivity analysis* has been carried for each of the 3 starting configurations: coaxial (C1.1 - Fig. 4.1), swirl of oxidizer SO1.1, swirl of fuel SF1.1. Red represents the fuel injection section from here onwards.

In the analysis the predicted chamber pressure (normalized over the nominal one, that is 4 bar) is monitored while the dimension of the mesh elements have been reduced gradually. From one mesh to the next a +75% increase in the number of elements was targeted, but it was a very loose target. The mesh is considered refined enough when the change in pressure between one mesh and the other is <0.5%.

Some locations have been slightly refined (i.e. smaller mesh elements) for higher accuracy, these are the places where the velocity gradients are expected to be higher than the rest of the chamber: near the throat, inside the injectors, at sharp turns. The dimensions of these refined locations have been proportionally adjusted too in the sensitivity analysis.

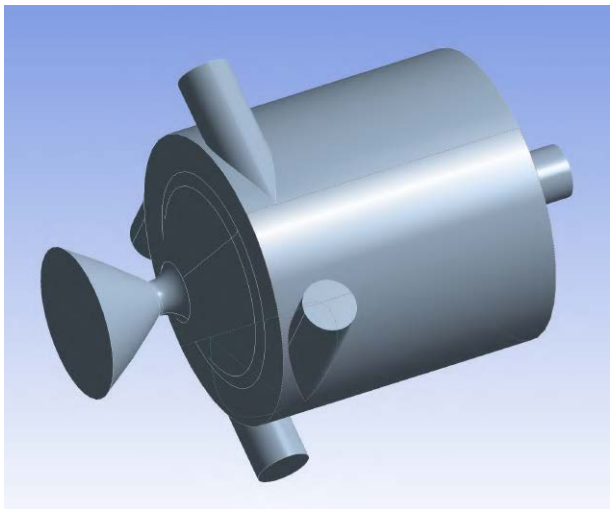

Figure 4.2: Configuration SO1.1.

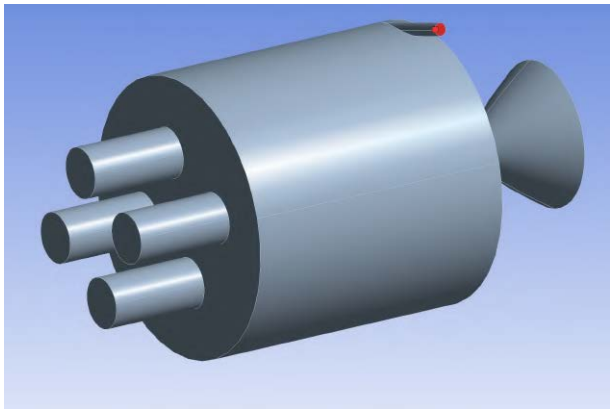

Figure 4.3: Configuration SF1.1.

4.5.2 Mesh sensitivity of configuration C1.1

The results of the mesh sensitivity analysis of the coaxial design C1.1 are summarized in Table 4.1 and Fig. 4.4. The very last mesh tested is identical to the previous one except for a refinement on the throat. The results confirmed the throat did not need any change.

All subsequent simulations of the coaxial kind featured around 1.5 million elements.

Table 4.1: Mesh sensitivity of configuration C1.1

Chamber pressure [Pa]	Normalized pressure	N. of elements	variation
335300	0.83825	230347	0%
325500	0.81375	481848	-2.92%
321900	0.80475	852229	-1.11%
321500	0.80375	1515943	-0.12%
321500	0.80375	1686726	0.00%

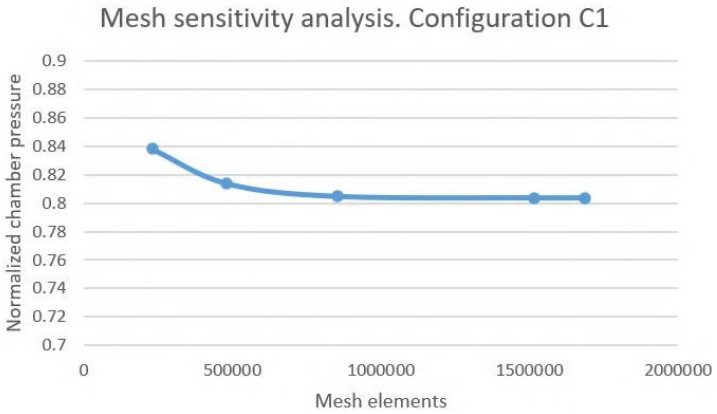

Figure 4.4: Configuration C1.1 mesh sensitivity analysis results.

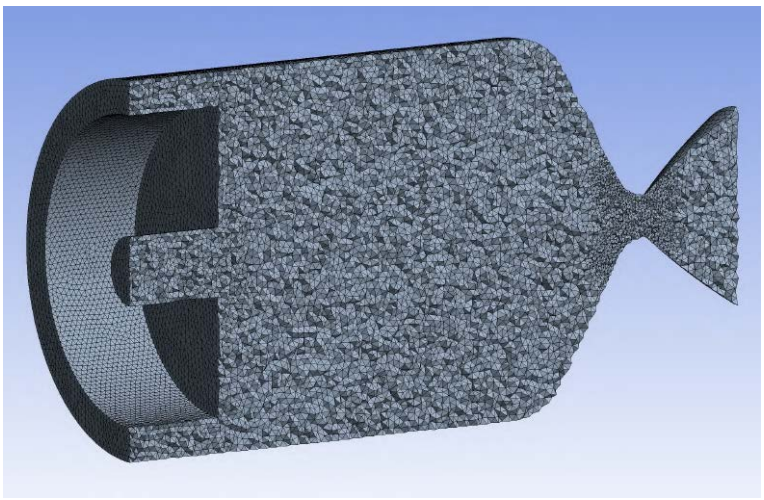

Figure 4.5: Internal mesh of configuration C1.1.

4.5.3 Mesh sensitivity of configuration SO1.1

The results of the mesh sensitivity analysis of the swirling oxidizer design SO1.1 is summarized in Table 4.1 and Fig. 4.4.

The subsequent simulations of the "swirl of oxidizer" kind featured around 2.2 million elements.

Table 4.2: Mesh sensitivity of configuration SO1.1

Chamber pressure [Pa]	**Normalized pressure**	**N. of elements**	**variation**
406800	1.017	223248	0%
407700	1.01925	344013	0.22%
411300	1.02825	574883	0.88%
414800	1.037	933899	0.85%
420800	1.052	1607096	1.45%
421300	1.053	2190580	0.12%

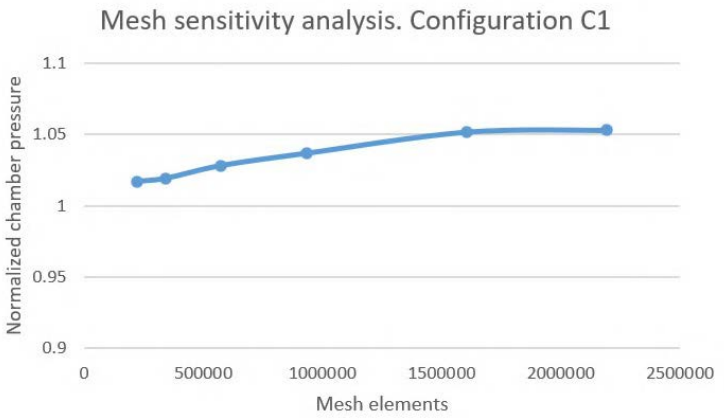

Figure 4.6: Configuration SO1.1 mesh sensitivity analysis results.

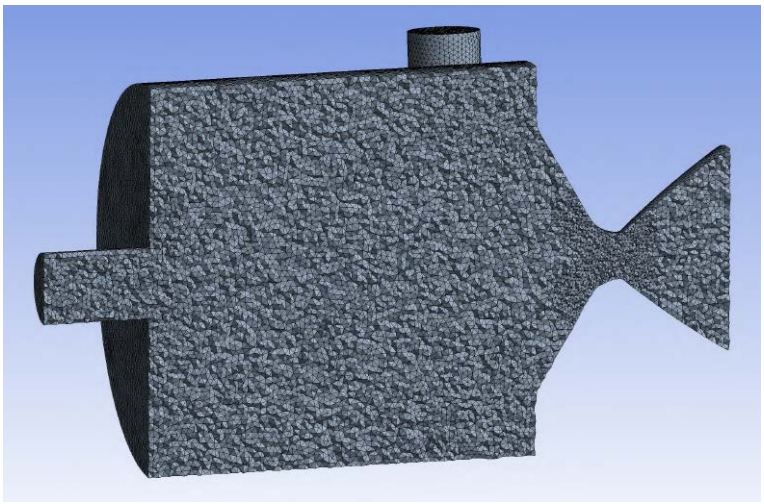

Figure 4.7: Internal mesh of configuration SO1.1.

4.5.4 Mesh sensitivity of configuration SF1.1

The results of the mesh sensitivity analysis of the swirling fuel design SO1.1 is summarized in Table 4.3 and Fig. 4.8.

This kind of design was not very successful and it was readily abandoned, the only 2 configurations simulated featured 2.1 and 2.0 million elements.

Table 4.3: Mesh sensitivity of configuration SF1.1

Chamber pressure [Pa]	Normalized pressure	N. of elements	variation
384100	0.96025	303047	0%
385700	0.96425	585007	0.42%
387600	0.96900	884859	0.49%
391000	0.97750	1272617	0.88%
393700	0.98425	1620778	0.69%
395700	0.98925	2100539	0.51%
396300	0.99075	2671512	0.15%

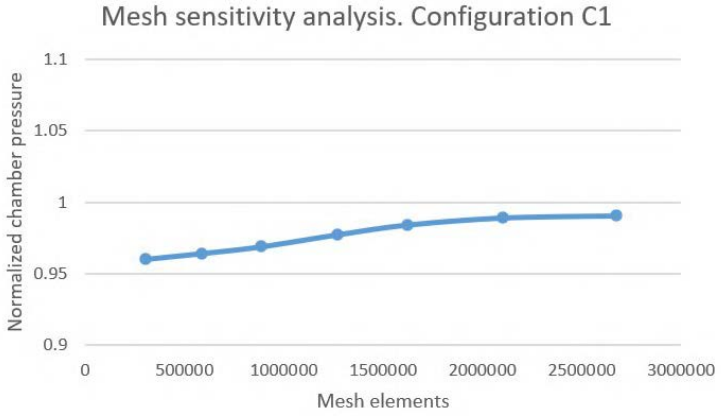

Figure 4.8: Configuration SF1.1 mesh sensitivity analysis results.

Figure 4.9: Internal mesh of configuration SF1.1.

4.5.5 Meshing of subsequent configurations

Being a very time-intensive task, the mesh analysis was not carried on for each of the configurations investigated, rather the dimensions of the elements found to be satisfactory in the 3 sensitivity analyses were used as the upper limit for the designs derived later on. This approach was deemed more beneficial because it allows to increase about 4 times the number of configurations tested in the same time frame with little risk of inaccuracy.

A mesh analysis was later done for the final two best configurations to confirm the invariability of the results found.

4.6 Inlet settings

For the inlets the following settings have been used in ANSYS CFX:

- subsonic
- mass flow rate (fuel): 0.044 g/s
- mass flow rate (oxidizer): 0.288 g/s
- normal to boundary
- turbulence intensity: medium (5%)
- static temperature (fuel): 298 K
- static temperature (oxidizer): 1020 K

4.7 Outlet settings

The outlet settings for all simulations are the following:

- subsonic
- average static pressure: 1000 Pa
- pressure profile blend: 0.5

The outlet pressure has been evaluated through a MATLAB script where the gas dynamics equations have been implemented. The predicted exit pressure for an expansion ratio $\epsilon = 19$ has been lowered and rounded up to 1000 Pa, to help avoid the formation of shock-waves during the solution.

4.8 Control points

To assess the characteristics of each configuration and to compare them methodically, it is necessary to set some standardized control points, or more precisely "control sections" since many characteristics need to be averaged on a section rather than just be taken on a point.

The sections represented in Fig. 4.10 are the locations where swirl number, temperature, pressure and chemical species have been evaluated. This data has been compared between the different configurations to assess the improvements from one configuration to the other, but it was also compared to the theoretical values (from the thermochemical software CPROPEP and the gas dynamics equations implemented in MATLAB) as an additional check. c^* efficiency has been estimated from the average pressure on the "chamber section".

The adiabatic flame temperature and the convective heat transfer coefficient was evaluated as an average on the whole wall surface (i.e. everything that is not an inlet nor an outlet), with a further sectioning of those parameters in these 3 zones: head surface, side chamber wall and nozzle.

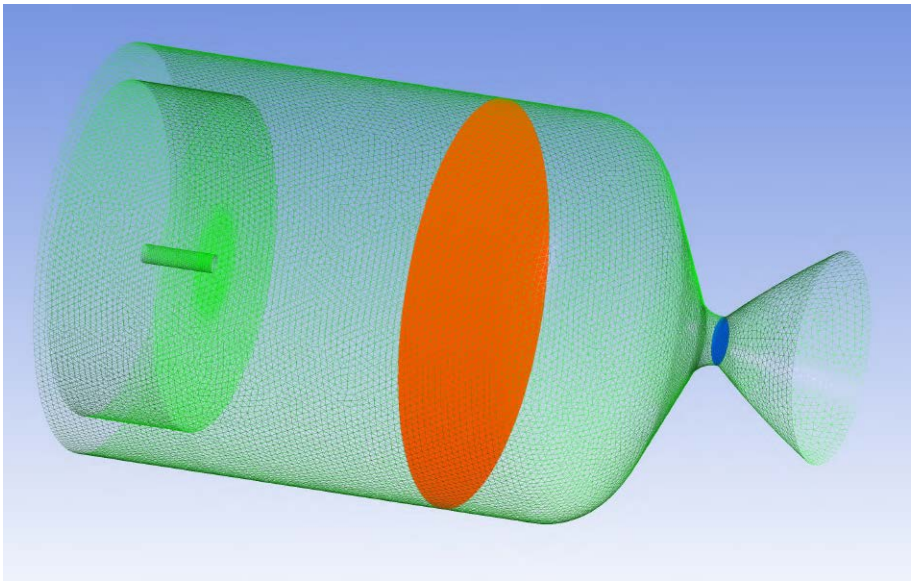

Figure 4.10: Control sections: chamber (orange) and throat (blue).

4.9 Control simulation with nozzle

To check the simulations were properly set and they could produce results very close to the theoretical ones, when proper mixing and sufficient residence time in the combustion chamber were assured, a control simulation was carried with a design featuring 4 unlike impinging injectors and a chamber with double the characteristic length chosen for the actual engine (Fig. 4.11). The results showed very little difference with the theoretical values at the control points (chamber, throat) and it predicted a 100.9% combustion efficiency (based on pressure).

The whole nozzle ($\epsilon = 100$) was restored on this configuration, to get a better evaluation of nozzle efficiency at a such small scale (high boundary layer losses were expected). Using Eq. 2.1 on the outlet section and by taking out the effect of combustion efficiency, it resulted a quite conservative 92.5% nozzle efficiency that was later used in the evaluation of I_{sp} for all the configurations.

The whole domain was represented by 3.84 million mesh elements and the solution required about 22 hours on a consumer-grade computer with a 12-core CPU (AMD Ryzen 3900X) with 32GB of RAM.

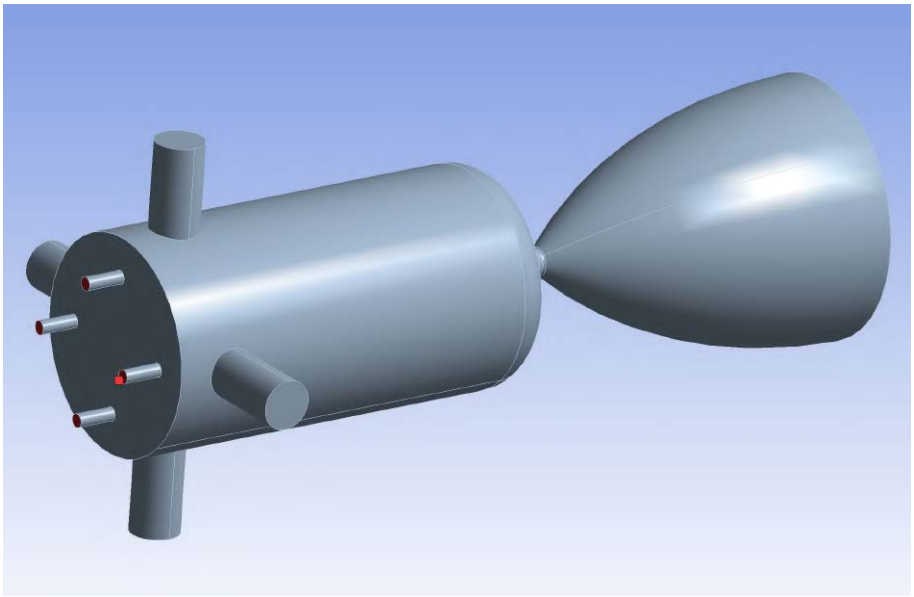

Figure 4.11: The special engine design for the control simulation. Red denotes the fuel injection points.

5 Results

5.1 Summary of results

A total of 46 injection configurations have been numerically tested using the commercial CFD software ANSYS CFX, 41 of those are illustrated in Fig. 5.1. In this summary scheme, beside every engine design there are some relevant data about it:

- Expected I_{sp} with expansion ratio=100.
- average fluid total temperature at the wall boundary, averaged on the whole fluid surface.
- maximum fluid total temperature at the wall boundary, anywhere on the whole fluid surface.
- convective heat transfer coefficient, averaged on the whole fluid surface.

To keep track of the different designs a unified naming format has been adopted:

AB.x.y.z

- *AB* denotes the *series*, it can be either C (coaxial), SO (swirl of oxidizer) or SF (swirl of fuel).
- x denotes the *sub-series*, which corresponds to an injection strategy: parallel streams, impinging, unconventional.
- y is the progressive number of the injection design. Until a satisfactory design is found, the design is varied with a trial-and-error procedure while taking into account what has been learned from the past simulations.
- z is the minor revision number. When a promising design was found, small adjustments were made to try to improve it. These take place in the form of slight dimensional changes. In Fig. 5.1 they were not represented to save some space, with the exception of the best performing minor revision.

Some swirling configurations (SO series) were outright excluded due to strong swirl ($S_N > 0.65$ in the chamber control section), others just produced inaccurate combustion efficiency estimates due to significant swirl ($0.5 < S_N < 0.65$).

The SF series has been abandoned very early (only 2 designs tried), because it was clear the fuel mass flow rate was too little compared to the oxidizer. A great amount of oxidizer inlets was needed and the fuel injector required a very small inlet section to maximize the injection

velocity, nevertheless very low swirl numbers resulted from using the smallest diameter that was deemed manufacturable (0.5 mm). Basically the 2 designs tried were non-swirling in reality and the thermals at the wall were unsatisfactory.

The best configurations coming out of this work were the C2.17 and the SO2.1.5. They are the ones with very high combustion efficiency, low total temperature at the wall and low convective heat transfer coefficient. These, along some noteworthy earlier designs will be described in the following pages.

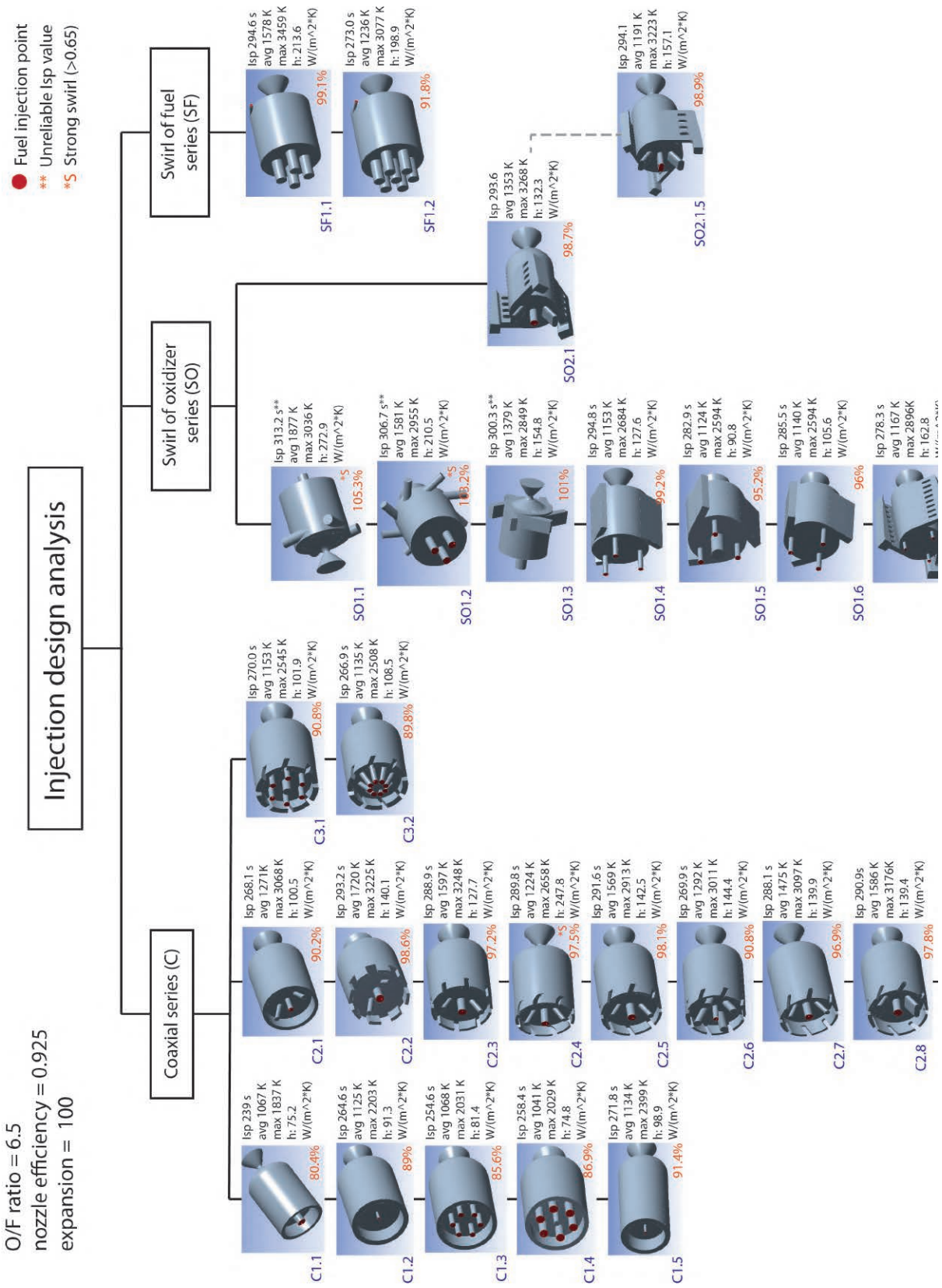

Figure 5.1: Visual summary of all the configurations reviewed in this work. (continues in the next page)

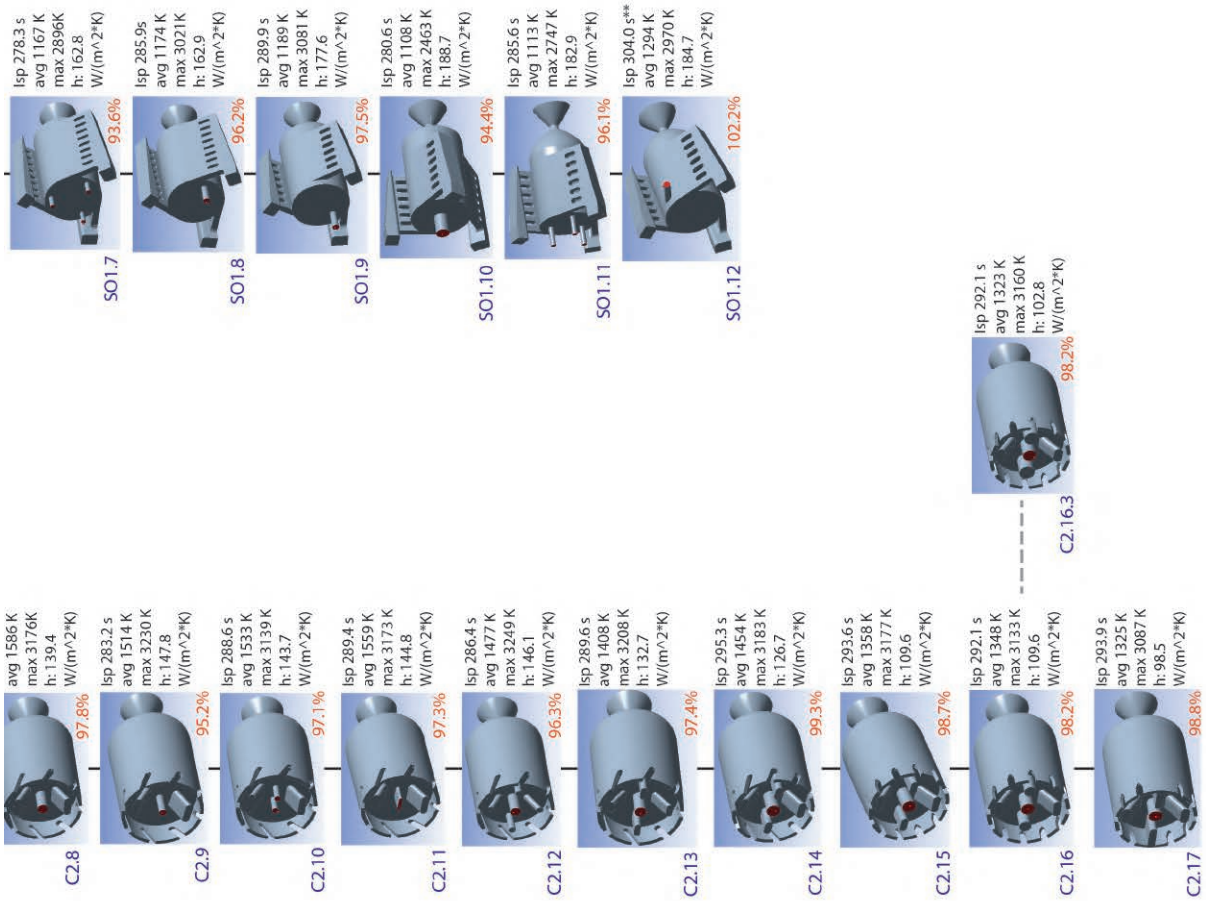

Figure 5.1: (continued from previous page) Visual summary of all the configurations reviewed in this work.

5.2 Coaxial injection series (C)

The coaxial series aimed to produce an oxidizer film cooling on the chamber wall, the opposite combination was simply impossible due to the low mass flow rate and higher density of the gaseous fuel at ambient temperature (while the decomposed HTP has a theoretical temperature of 1020 K and lower density). A slow laminar flow is desired near the wall, however it is also important the oxidizer mixes totally with the fuel before it passes the nozzle throat.

5.2.1 Coaxial straight injection (C1)

5.2.1.1 Configuration C1.1

The first and simplest design was the C1.1 shown in Fig. 5.2: a circular annulus for the oxidizer and a central axially-directed fuel injector. A great amount of fuel and oxidizer did not mix due to the slow laminar flow (Fig. 5.3), resulting in a terrible combustion efficiency of 80.4%.

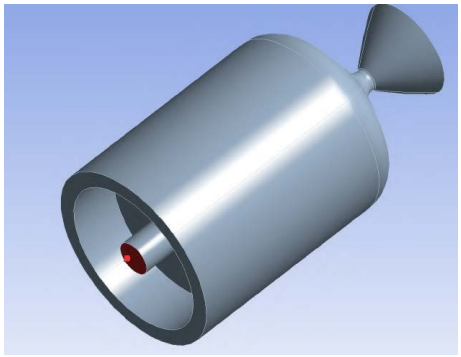

Figure 5.2: Coaxial configuration C1.1: injectors. Fuel injection in red.

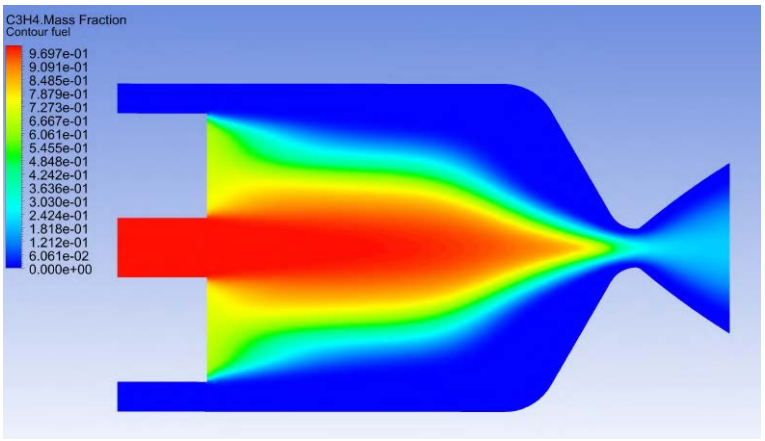

Figure 5.3: Coaxial configuration C1.1: fuel mass fraction in the engine.

5.2.1.2 Configuration C1.2

Trying to check if a fast and turbulent jet of fuel could help the mixing issue encountered with the design C1.1, in C1.2 (Fig. 5.4) the fuel injector has been reduced to the minimum allowable diameter of 0.5 mm. The combustion efficiency improved to 89%, which was still underwhelming. This meant the mixing improved due to turbulence (Fig. 5.5) but not nearly enough to be considered a viable solution. To check if a longer and slimmer combustion chamber could achieve a reasonable combustion efficiency with this design, configuration C1.5 was made but failed in its purpose, improving the efficiency by a mere 2.4% ($\eta_{c^*} = 91.4\%$).

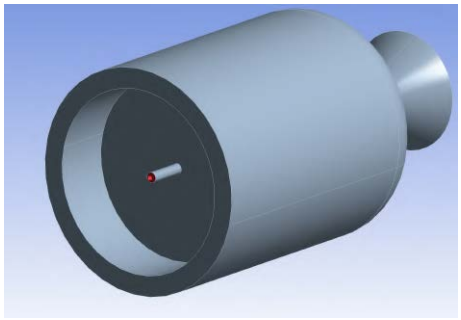

Figure 5.4: Coaxial configuration C1.2: injectors. Fuel injection in red.

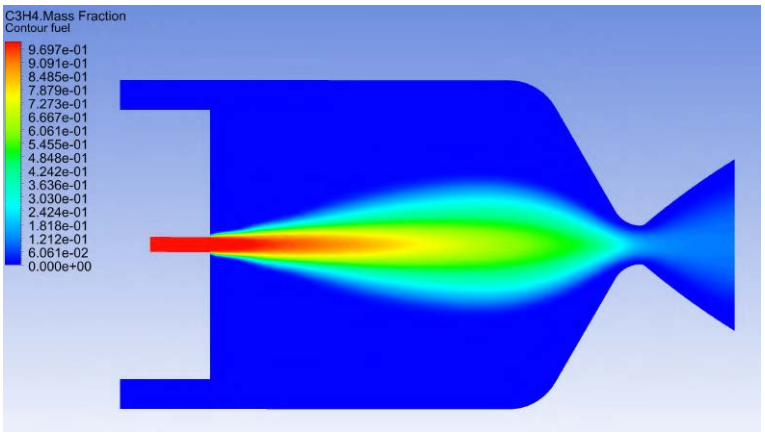

Figure 5.5: Coaxial configuration C1.2: fuel mass fraction in the engine.

5.2.1.3 Configuration C1.4

This is a trial of the "shower head" injection performance, to help the mixing a central small oxidizer was placed to avoid the build-up of too much fuel at the center.

The configuration is shown in Fig. 5.6.

As with all the other coaxial designs with axially directed injection, the thermals (average total temperature near-wall, convective heat transfer coefficient) were excellent but at the cost of very low combustion efficiency. The central oxidizer injector did not provide enough turbulence to

disrupt the flow of fuel and mix effectively, it resulted in a $\eta_{c^*} = 86.9\%$.

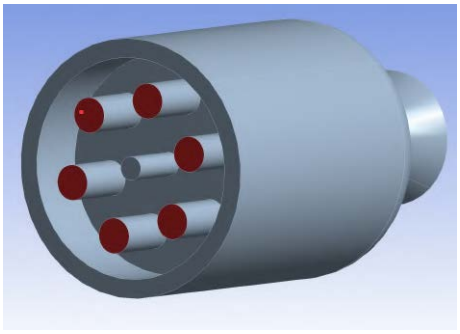

Figure 5.6: Coaxial configuration C1.4: injectors. Fuel injection in red.

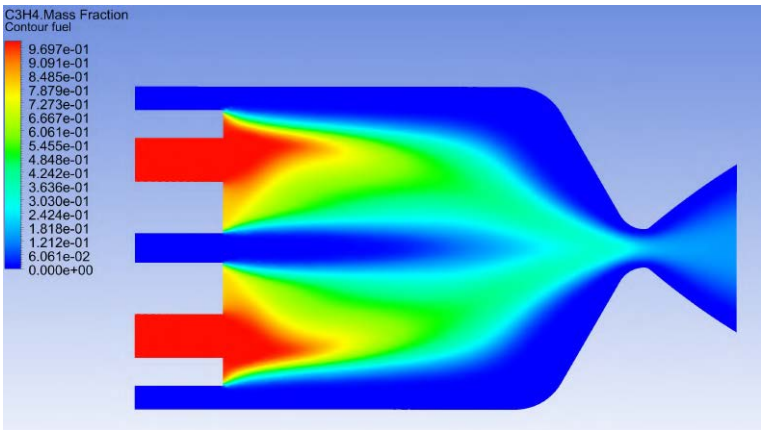

Figure 5.7: Coaxial configuration C1.4: fuel mass fraction in the engine.

5.2.2 Coaxial impinging injection (C2)

This is the most successful series, resulting almost always in decent combustion efficiencies with low to zero swirl number (some configurations implemented a light swirl). The annulus width has been reduced to divert more oxidizer to the impinging injectors. Only triplet and quintuplet impinging designs have been tried to avoid the formation of hot spots near the wall in case of important manufacturing imperfections: compared to doublets, having more injectors in a symmetrical pattern should avoid the stream of fuel not encountering at all the oxidizer.

5.2.2.1 Configuration C2.1

As pictured in Fig. 5.4, it is a very simple triplet impinging design, with 2 oxidizer jets and 1 fuel jet, all of them 1 mm of base diameter. The oxidizer jets featured a low velocity (11 m/s), comparable to the mean axial velocity in the combustion chamber. Overall, the momentum of the 2 oxidizer jets was insufficient to disrupt the fuel jet and achieve efficient mixing (Fig. 5.9). The efficiency was 90.2%.

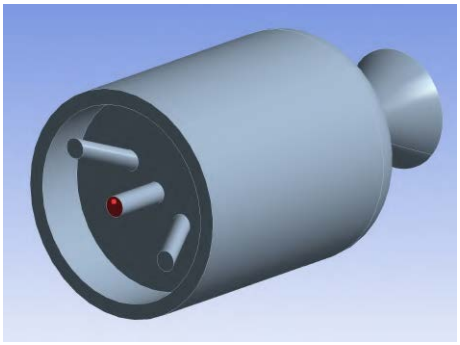

Figure 5.8: Coaxial configuration C2.1: injectors. Fuel injection in red.

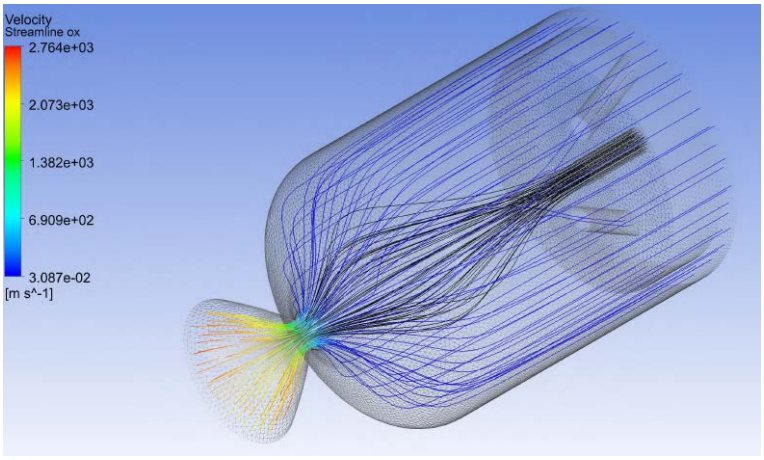

Figure 5.9: Coaxial configuration C2.1: streamlines in isometric view. Oxidizer is rainbow color-coded, fuel is black.

5.2.2.2 Configuration C2.2

To restrict the oxidizer flow in the annulus and divert more of it to the impinging injectors (without using different feed pressures that would increase the complexity of the feed line design) several "cuts" were added to the annulus and its width reduced from 0.75 mm (in configuration C2.1) to 0.6 mm. The fuel injector was enlarged to 1.5 mm in diameter.

This was the first design to achieve a high combustion efficiency (98.6%). Thanks to the increased momentum of the 2 oxidizer jets and the decreased momentum of the fuel one, some recirculation was achieved (Fig. 5.11). However the cuts in the annulus also created high temperature trails at the wall (Fig. 5.12).

In the configuration C2.3 these cuts were made smaller but only a small reduction in average wall temperature and convective heat coefficient was achieved, counterbalanced by a slightly lower combustion efficiency.

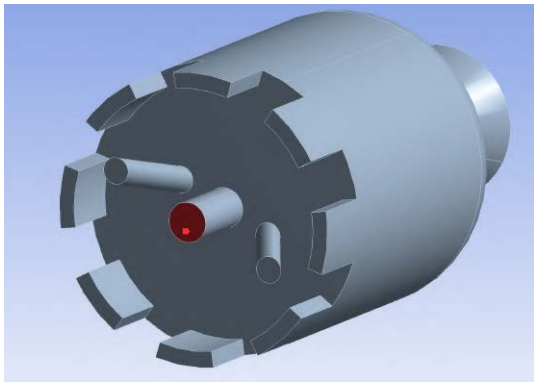

Figure 5.10: Coaxial configuration C2.2: injectors. Fuel injection in red.

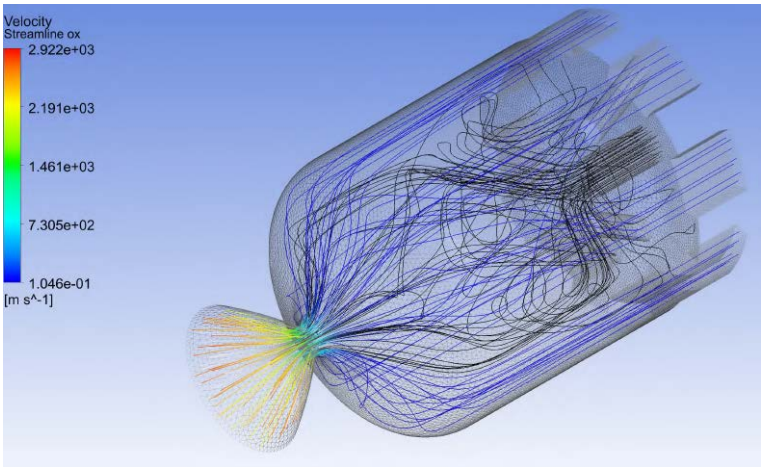

Figure 5.11: Coaxial configuration C2.2: streamlines in isometric view. Oxidizer is rainbow color-coded, fuel is black.

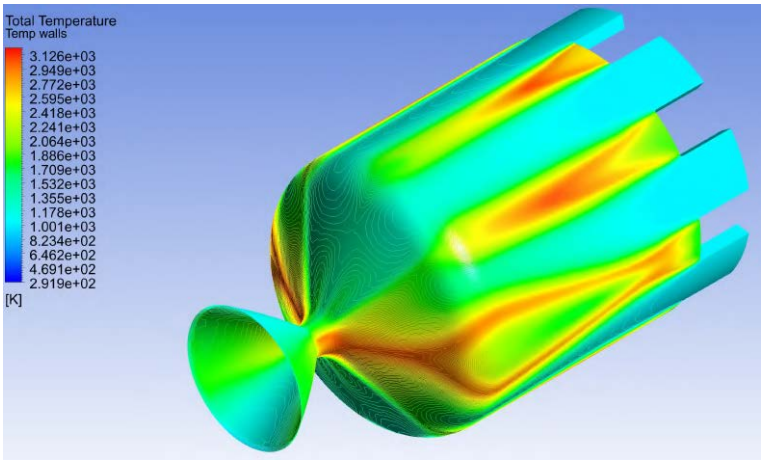

Figure 5.12: Coaxial configuration C2.2: total temperature of the fluid at the wall boundary.

5.2.2.3 Configuration C2.5

C2.5 is basically the configuration C2.3 with a moderate swirl ($S_N = 0.374$) created by the oblique cuts in the annulus. This brought the average wall temperature down by about 150 K while keeping the combustion efficiency basically intact (98.1%). This swirl strategy will be kept for many following configurations, then dismissed when the oxidizer impinging injectors became so large they had most of the mass flow and the annulus produced a negligible swirl anyway. In Fig. 5.14 and 5.15 we can see the film cooling achieved.

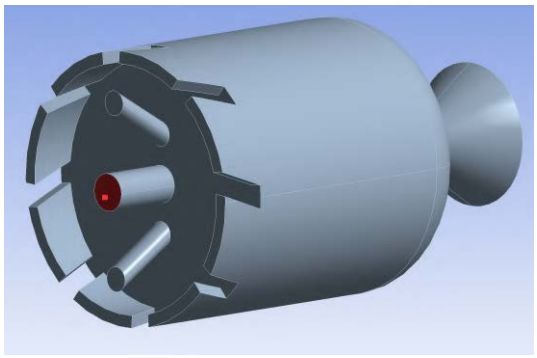

Figure 5.13: Coaxial configuration C2.5: injectors. Fuel injection in red.

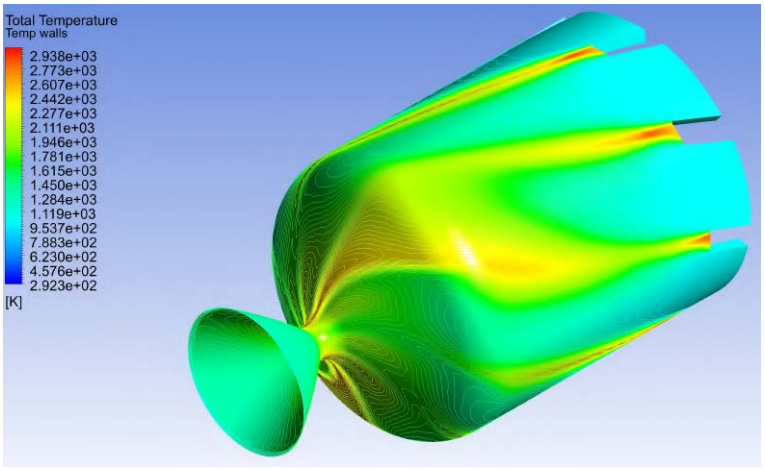

Figure 5.14: Coaxial configuration C2.5: total temperature of the fluid at the wall boundary.

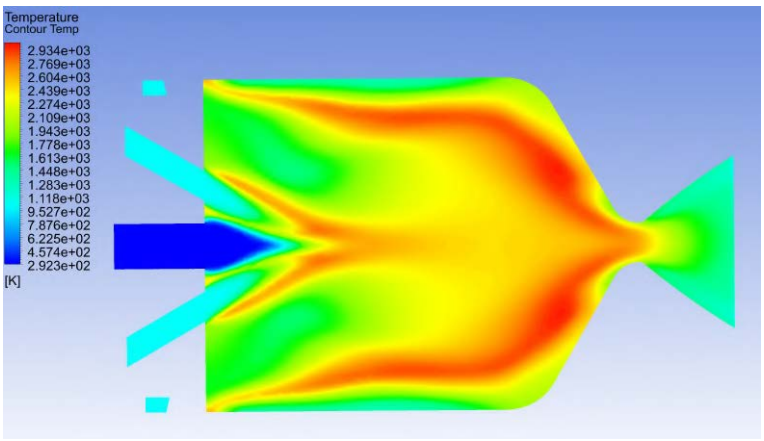

Figure 5.15: Coaxial configuration C2.5: internal temperature, section of the engine.

5.2.2.4 Configuration C2.6

This configuration was an attempt with an impinging quintuplet, but it just resulted in the fuel stream being confined along the center axis (Fig. 5.17) and reducing the mixing effect seen in the impinging triplet that separated the fuel stream in two. η_{c^*} is just 90.8%.

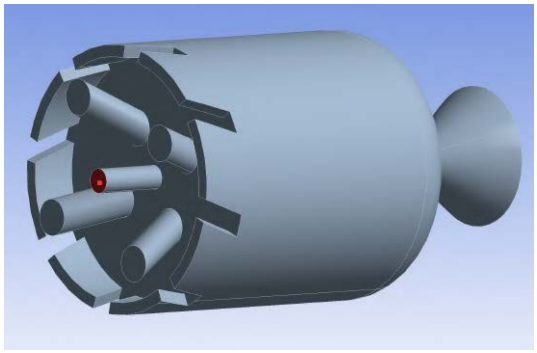

Figure 5.16: Coaxial configuration C2.6: injectors. Fuel injection in red.

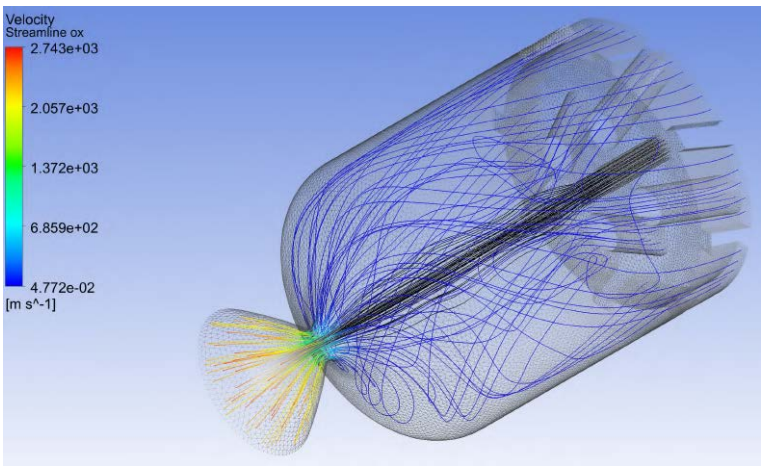

Figure 5.17: Coaxial configuration C2.6: streamlines in isometric view. Oxidizer is rainbow color-coded, fuel is black.

5.2.2.5 Configuration C2.8

Here the impinging oxidizer injectors received a new "slot" profile in place of the old circular one, this addressed at the same time the need to have more impinging oxidizer mass flow and the issue of manufacturing imprecision on impinging designs. The large slotted design is much more tolerant of misalignment and partial occlusion.

Also the cuts in the annular section have been receded to mitigate the "wake turbulence" effect that created hot spots behind the trailing edge of the cuts, a modification already introduced in C2.7. Comparing Fig. 5.19 with Fig. 5.14 we can see it had the desired effect on the wake turbulence generated by the cuts but the reduced mass flow in the annular section (due to the greatly enlarged oxidizer impinging injectors) allows some of the fuel to burn too close to the wall, resulting in two large high temperature areas.

The combustion efficiency (97.8%), the convective coefficient and the average temperature at the wall, were basically the same as configuration C2.5.

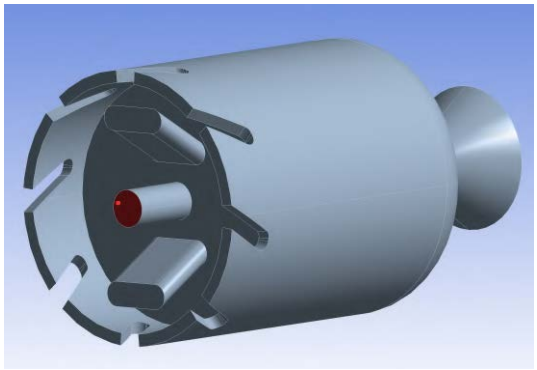

Figure 5.18: Coaxial configuration C2.8: injectors. Fuel injection in red.

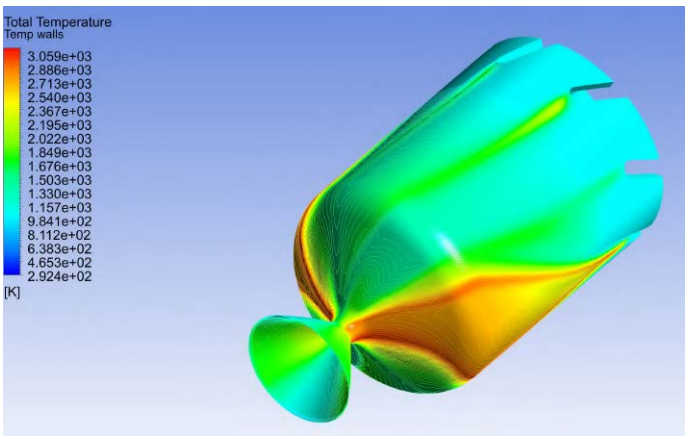

Figure 5.19: Coaxial configuration C2.8: total temperature of the fluid at the wall boundary.

5.2.2.6 Configuration C2.13

This configuration features a new injection strategy (Fig. 5.20) highly improving the thermals: the impinging triplet divides the stream in half, two lateral and parallel jets of oxidizer further divide each stream in half again, also creating vortexes that are confined away from the wall.

In Fig. 5.21, there a view from above, with the parallel oxidizer injectors highlighted by the grey horizontal plane (fictitious, added just to make streamlines easier to visualize).

In Fig. 5.22, the engine is seen from the same perspective as Fig. 5.20, with a grey vertical plane that passes through the impinging oxidizer injectors.

The resulting engine has a combustion efficiency of 97.4%, discretely low average temperature at the walls (1408 K) without hot spots (Fig. 5.23) and an acceptable convective heat transfer coefficient of 132 $W/(m^2K)$. The swirl is so low it is effectively non-swirling ($S_N = 0.05$).

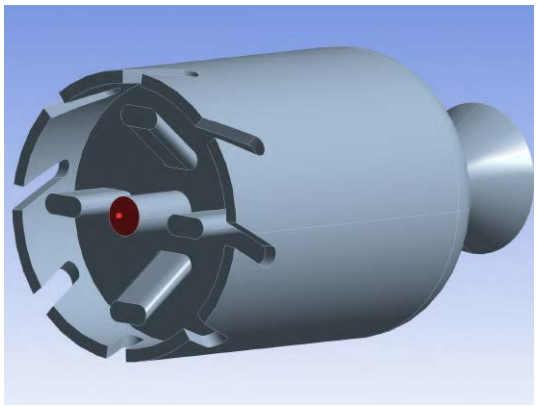

Figure 5.20: Coaxial configuration C2.13: injectors. Fuel injection in red.

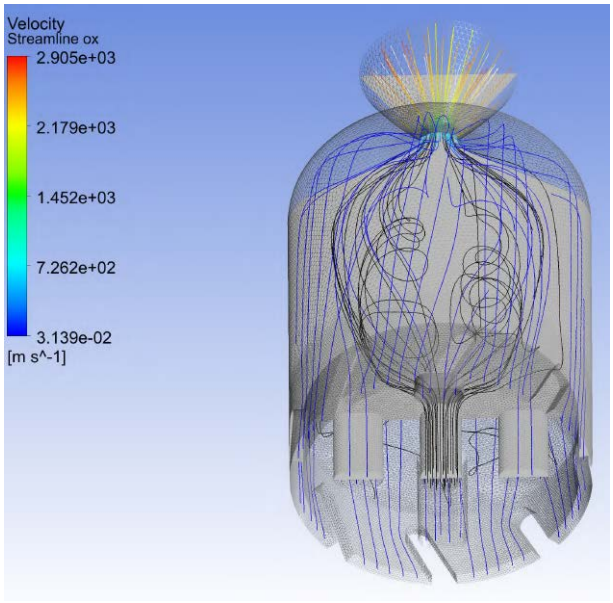

Figure 5.21: Coaxial configuration C2.13: streamlines, view from "above". Oxidizer is rainbow color-coded, fuel is black. The horizontal plane in grey is added for visual clarity.

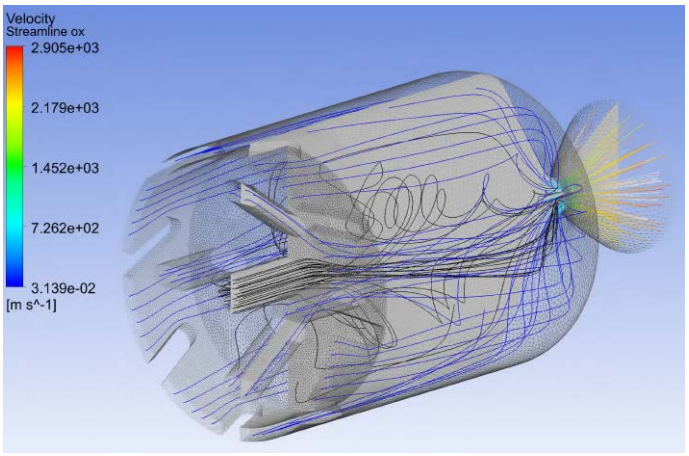

Figure 5.22: Coaxial configuration C2.13: streamlines, view from the "side". Oxidizer is rainbow color-coded, fuel is black. The vertical plane in grey is added for visual clarity

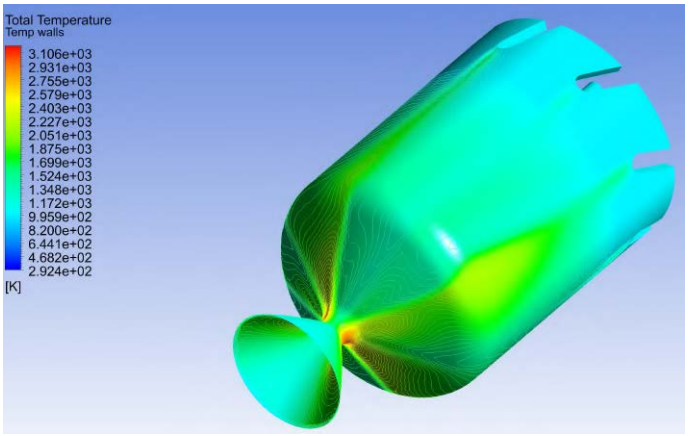

Figure 5.23: Coaxial configuration C2.13: total temperature of the fluid at the wall boundary.

5.2.2.7 Best coaxial configuration: C2.17

Pictured in Fig. 5.24, this is the best non-swirling configuration. The injection system is very much similar to the aforementioned C2.13, but the parallel injectors here are "fused" together with the annular section to ease manufacturing and increase oxidizer mass flow in the two zones where it is needed. The same principle applies: 2 impinging oxidizer injectors (angle with fuel jet: 35°) divide the central fuel jet in 2 streams, each of these fuel streams encouters one of the 2 parallel oxidizer jets and gets divided once more. Four vortices of fuel are created in the center (Fig. 5.27), mixing effectively the propellants (Fig. 5.28, 5.29), while the annulus provides a film cooling to the side chamber wall.

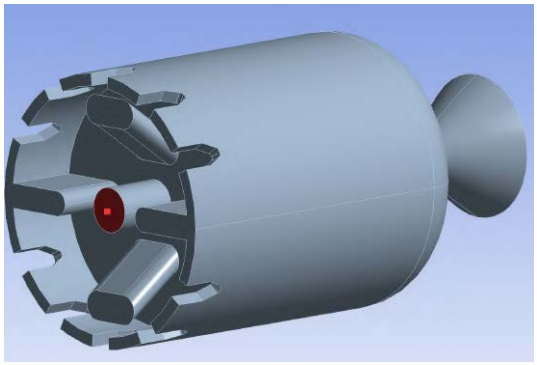

Figure 5.24: Coaxial configuration C2.17: injectors. Fuel injection in red.

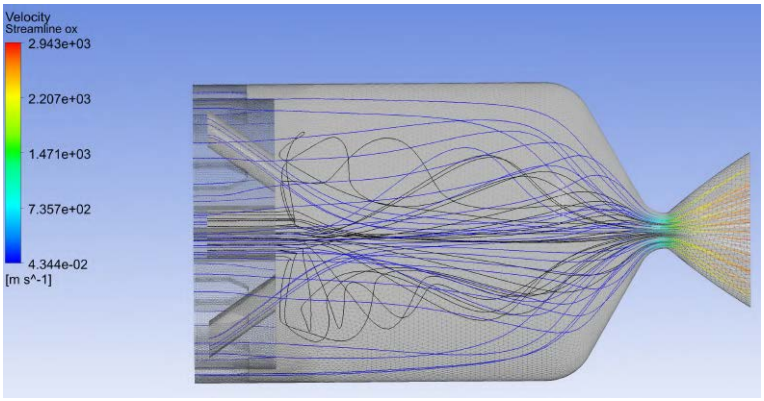

Figure 5.25: Coaxial configuration C2.17: streamlines, view from "side". Oxidizer is rainbow color-coded, fuel is black. The vertical plane in grey is added for visual clarity.

A combustion efficiency of 98.8% is derived from this simulation, leading to an expected I_{sp} of 293.9 seconds. The film cooling achieved is very effective, without any important hot spots on the side wall nor the divergent section of the nozzle (Fig. 5.30). The average total temperature near the wall is just 1348 K, coupled with a low convective heat transfer coefficient of 109.6 $W/(m^2K)$.

An advantage of the "cuts" in the annulus is that they provide structural stiffness to the injector

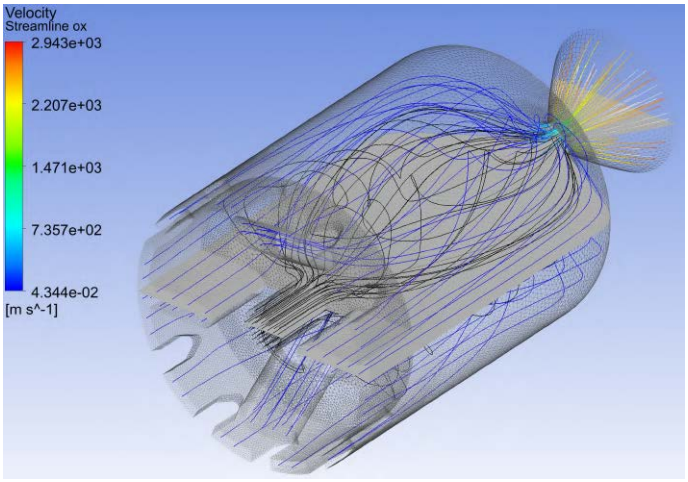

Figure 5.26: Coaxial configuration C2.17: streamlines, isometric view. Oxidizer is rainbow color-coded, fuel is black. The horizontal plane in grey is added for visual clarity.

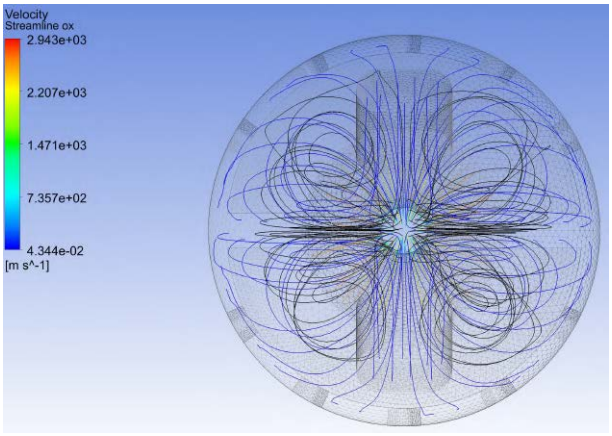

Figure 5.27: Coaxial configuration C2.17: streamlines, front of the engine view. Oxidizer is rainbow color-coded, fuel is black.

plate. They also help straighten the oxidizer flow path should the feed system introduce any deviation at the inlet.

The mesh used featured 1.9 million elements, to check if this number of elements was enough, a 2.96 million elements mesh was also tried and the chamber pressure increased just by 0.25%, which is negligible.

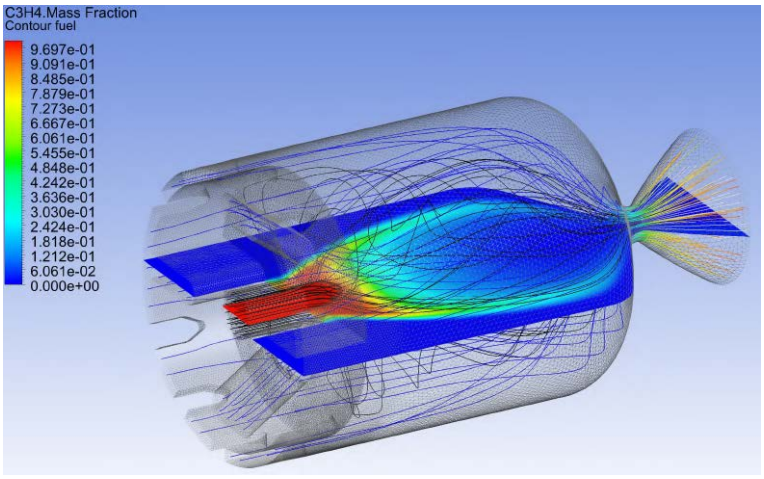

Figure 5.28: Coaxial configuration C2.17: streamlines and fuel mass fraction.

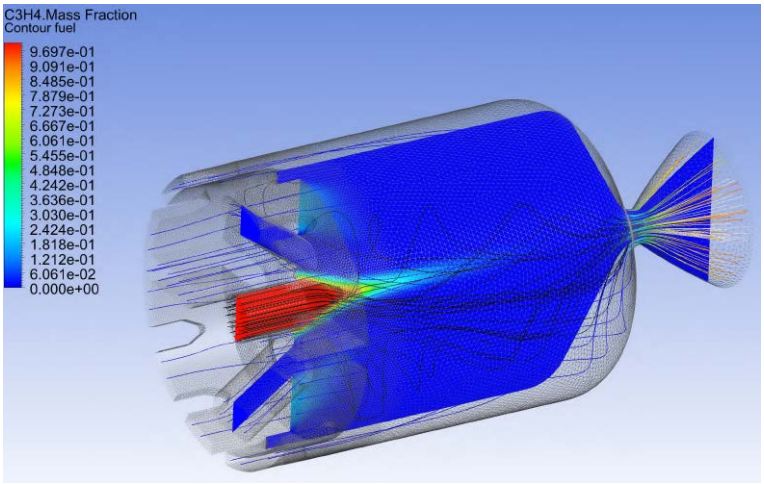

Figure 5.29: Coaxial configuration C2.17: streamlines and fuel mass fraction.

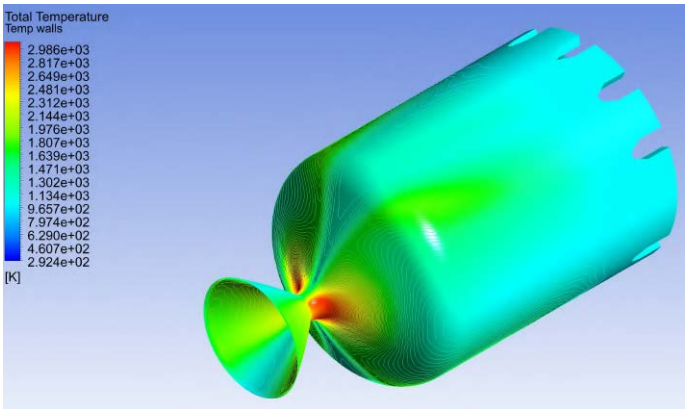

Figure 5.30: Coaxial configuration C2.17: total temperature of the fluid at the wall boundary. Isometric view

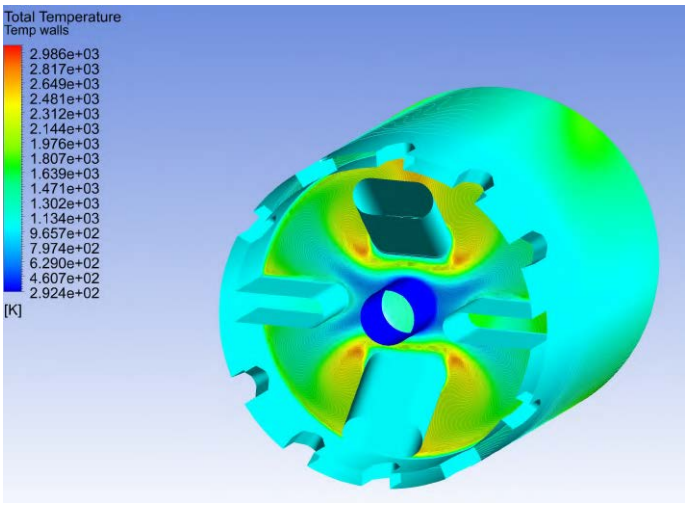

Figure 5.31: Coaxial configuration C2.17: total temperature of the fluid at the wall boundary. Front view

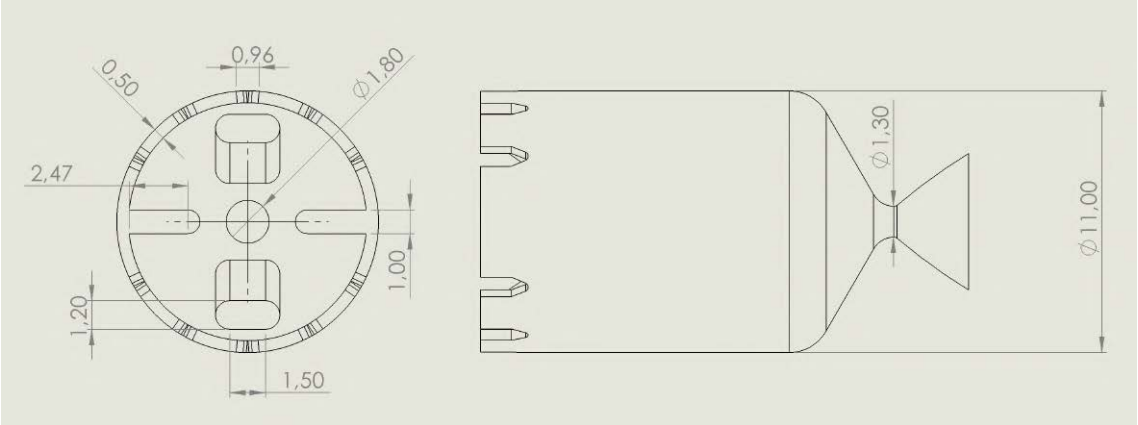

Figure 5.32: Coaxial configuration C2.17: dimensions and details of the injector plate.

5.2.3 Coaxial unconventional injections (C3)

Two configuration have been tried and they both resulted in a low combustion efficiency of about 90%. C3.1 was the last attempt with the "shower head" injector plate, but combining it with the swirl ring (Fig. 5.33). It did not seem to make much difference when compared to the previous shower head configuration C1.4.

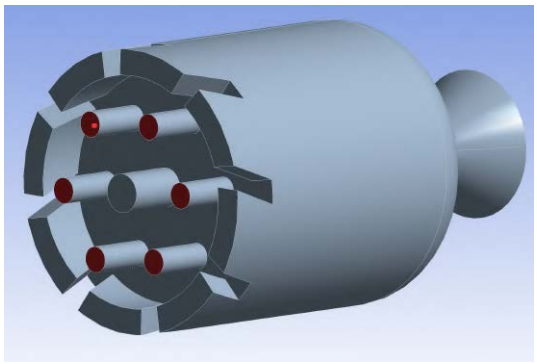

Figure 5.33: Coaxial configuration C3.1: injectors. Fuel injection in red.

C3.2 impinged the fuel jets directly to the annulus (Fig. 5.35), but the low momentum of the fuel made it very ineffective in actually penetrating the mantle of oxidizer.

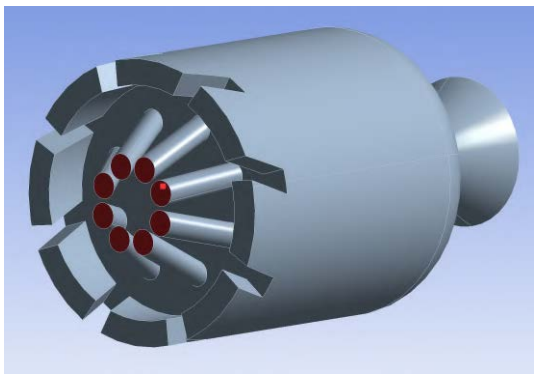

Figure 5.34: Coaxial configuration C3.2: injectors. Fuel injection in red.

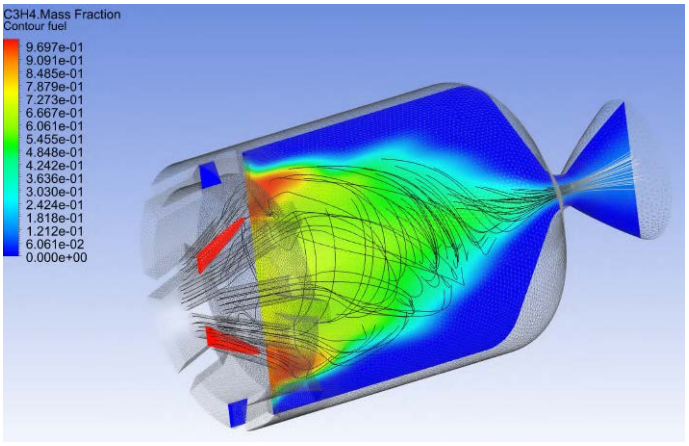

Figure 5.35: Coaxial configuration C3.2: streamlines (fuel) and fuel mass fraction.

5.3 Swirl of oxidizer series (SO)

This series was inspired by the *Vortex Combustion Cold-Wall* (VCCW) design proposed and tested by Chiaverini et al. [24] [25]. In that concept (Fig. 5.36) the oxidizer is tangentially injected at the bottom of the combustion chamber while the fuel at the top. Due to the angular momentum, the oxidizer will travel from the bottom to the top where it will mix with the fuel and start traveling back toward the bottom (nozzle). This motion creates two coaxial vortexes and the combustion will be confined in the inner one. The outer vortex is called *mantle* and the inner one *core*.

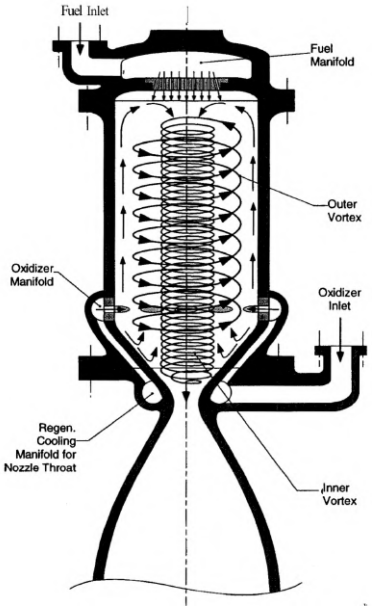

Figure 5.36: VCCW design concept.

To help contain the mantle from flowing partially out of the nozzle directly, there should be a flat bottom base with the divergent part of the nozzle starting at the same radial coordinate as the radius of the core. To predict the latter, an analytical inviscid fluid model developed by Majdalani [37] was used and the resulting nozzle has been used on configurations SO1.1 through SO1.10 (visible in Fig. 5.37).

However for such a small size engine, a design with oxidizer injectors wrapping completely or most of the side wall seemed to make more sense, providing better thermal insulation while reducing the swirl number due to the lower injection velocity. Therefore from configuration SO1.4 onwards the VCCW concept was scrapped for this work.

5.3.1 Swirl of oxidizer non-impinging (SO1)

5.3.1.1 Configuration SO1.1

The first design of the series was made as simple as possible: 4 tangential oxidizer injectors at the bottom and a single axially-directed fuel injector on the head.

The VCCW double coaxial vortex was achieved (Fig. 5.39), mixing very effectively all the fuel available (Fig. 5.40), but the high injection velocity of the oxidizer resulted in a very high $S_N = 1.54$ which is not within the intended limits of this thesis. In addition to the issues of high swirl already mentioned, the high tangential velocity also mixed the propellants too soon, leaving the top half of the chamber without the cool oxidizer mantle (Fig. 5.41).

The subsequent designs (SO1.2, SO1.3) tried to decrease this velocity by increase the injection points and surfaces, but those designs made the bottom of the chamber too crowded with injectors, without getting a swirl number below 0.5 or an estimated efficiency based on pressure below 100%.

For this reason the VCCW design was abandoned once for all with the configuration SO1.4, where the oxidizer injectors were covering the whole side wall. This approach is unfeasible for larger engines but it makes sense for a micro-propulsion system.

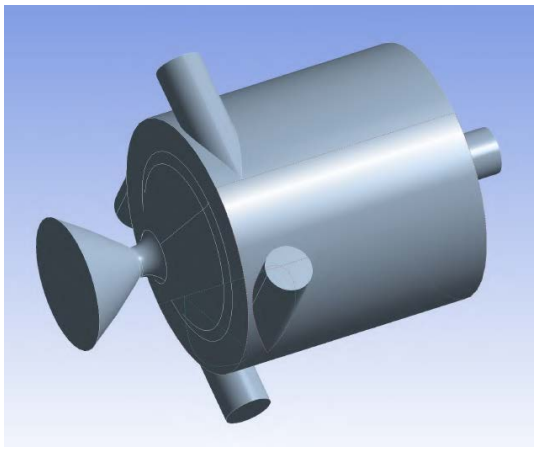

Figure 5.37: Swirl of oxidizer configuration SO1.1: injectors. Fuel injector is on head, central and axial.

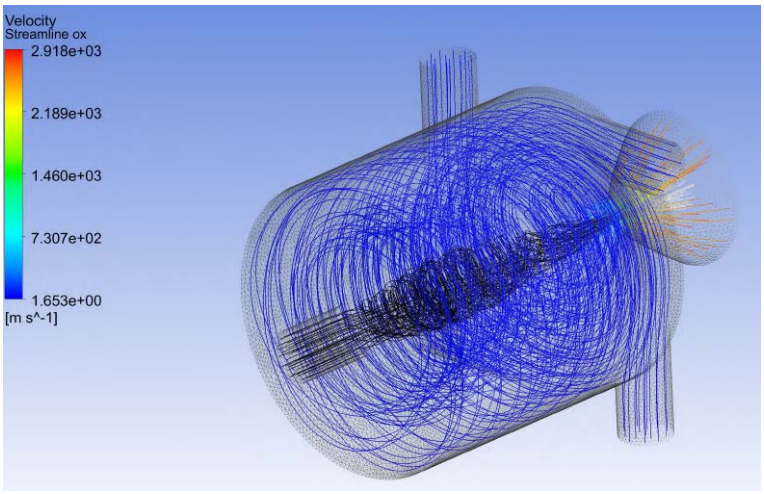

Figure 5.38: Swirl of oxidizer configuration SO1.1: streamlines. Oxidizer is rainbow color-coded, fuel is black.

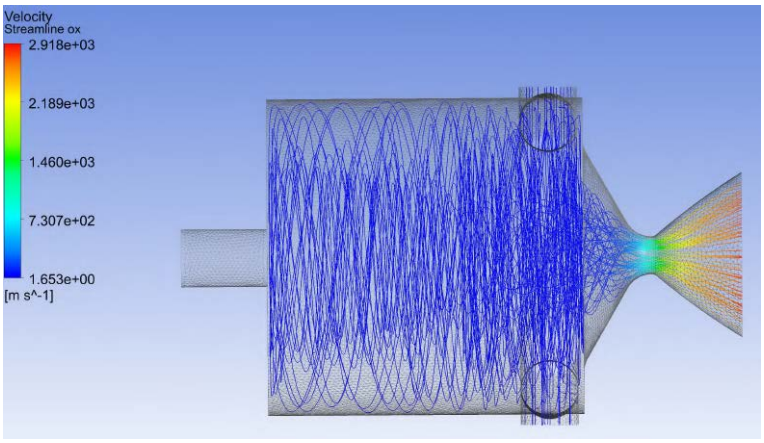

Figure 5.39: Coaxial configuration SO1.1: streamlines. Only oxidizer.

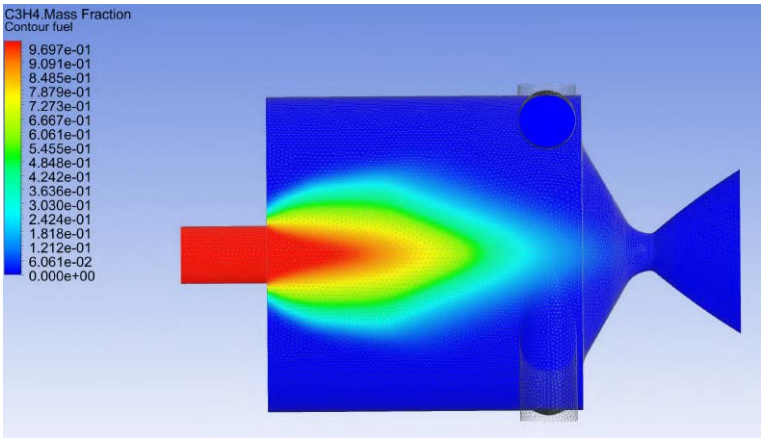

Figure 5.40: Swirl of oxidizer configuration SO1.1: fuel mass fraction.

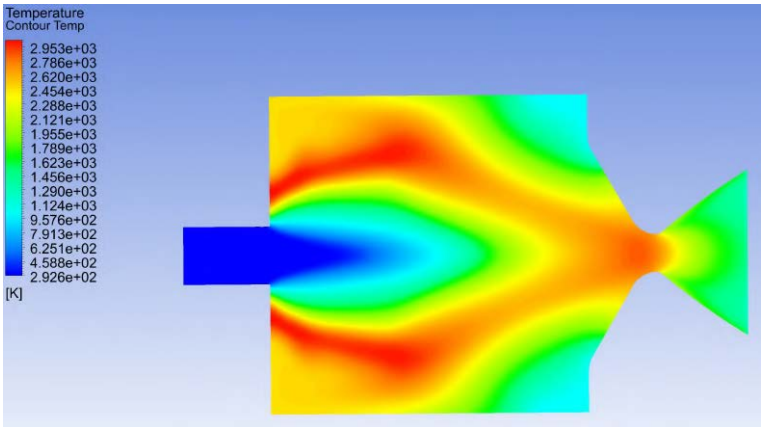

Figure 5.41: Swirl of oxidizer configuration SO1.1: temperature profile inside the engine.

5.3.1.2 Configuration SO1.4

The numerous tangential injectors seen in the VCCW designs have been replaced by 3 rectangular injectors (10x1.2 mm) covering almost the whole side wall. The fuel injectors are 3 straight holes, their positioning has been varied in the following configurations (SO1.5, SO1.6) but it did not seem to be very relevant for the combustion efficiency.

The thermals at the wall boundary are excellent (Fig. 5.46), but the swirl is still quite high ($S_N = 0.61$), therefore the 99.2% efficiency estimate based on chamber pressure could be slightly inaccurate, anyway the 2.5% mass fraction of residual fuel at the throat section indicates a very good mixing and combustion took place.

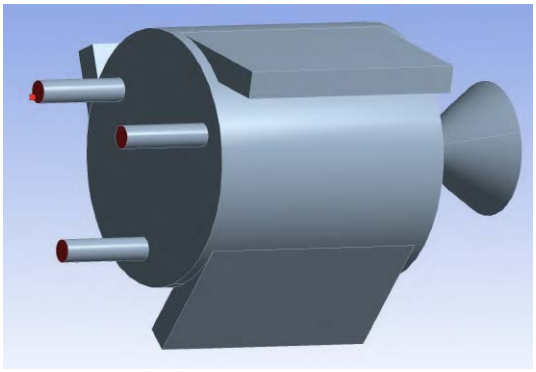

Figure 5.42: Swirl of oxidizer configuration SO1.4: injectors. Fuel injector is on head, central and axial.

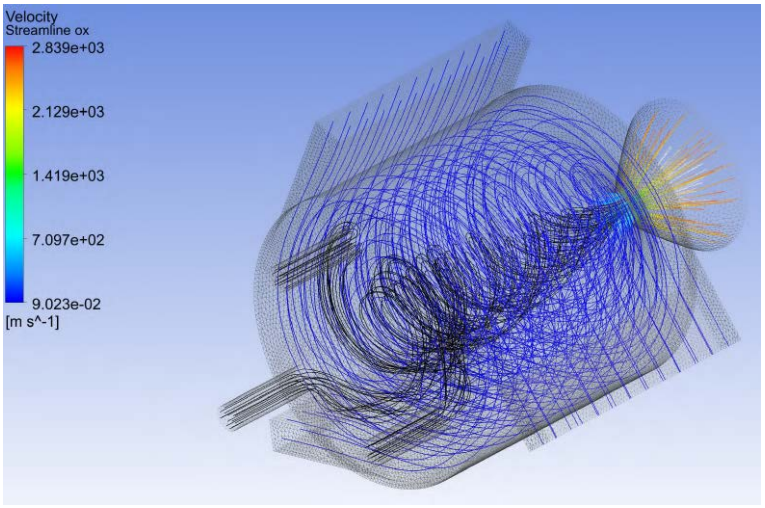

Figure 5.43: Swirl of oxidizer configuration SO1.4: streamlines. Oxidizer is rainbow color-coded, fuel is black.

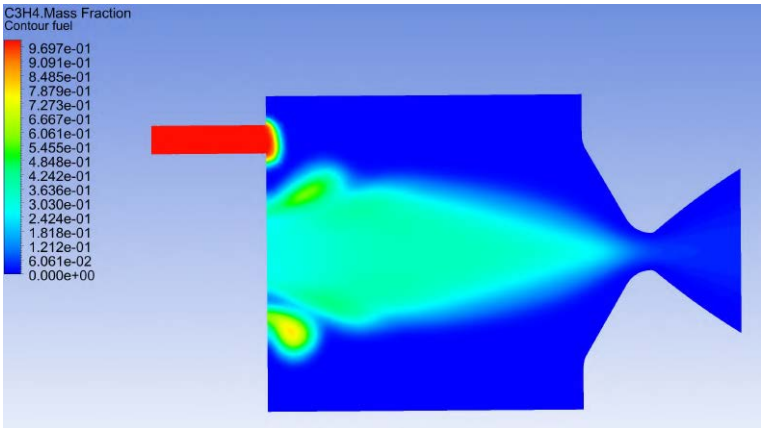

Figure 5.44: Swirl of oxidizer configuration SO1.4: fuel mass fraction.

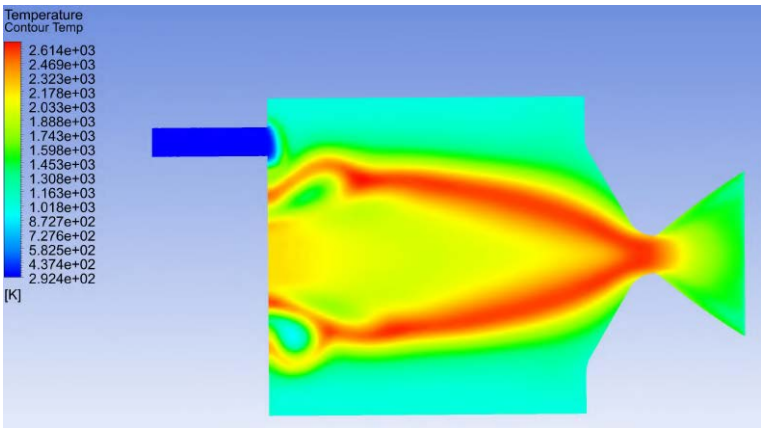

Figure 5.45: Swirl of oxidizer configuration SO1.4: temperature profile inside the engine.

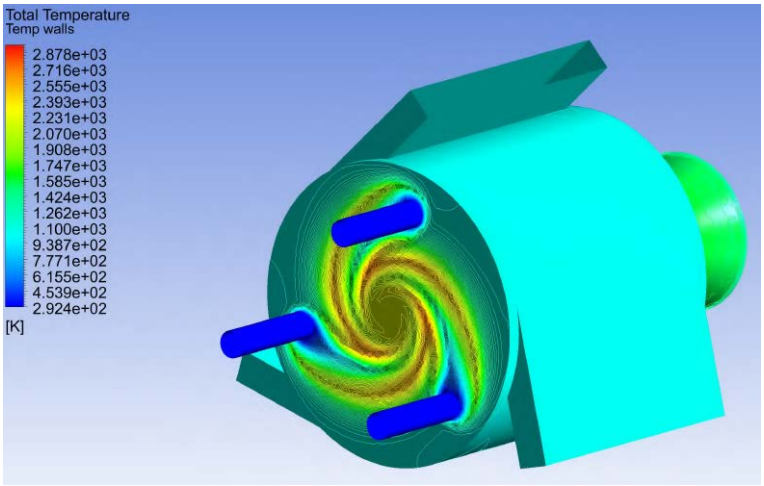

Figure 5.46: Swirl of oxidizer configuration SO1.4: total temperature of the fluid at the wall boundary.

5.3.1.3 Configuration SO1.7

The length to diameter ratio (L/D) of the combustion chamber has been increased from 1 to 1.5, keeping the same L^*, for 3 reasons:

- decrease of the head surface, which is inevitably hotter than the side wall in these swirling designs, being the injection location for the fuel.
- reduction of the angular momentum arm due to the oxidizer being injected closer to the central axis.
- increase of the side wall length to be used for injection, another contributing factor in reducing the excessive swirl.

The rectangular tangential injectors are now more realistically designed as a possible actual implementation. In Fig. 5.47 this feed system is visible: the oxidizer is injected in a large canal that distributes the flow along the side wall, restrictive slots are placed here to create a slight pressure loss allowing a more uniform mass flow along the tangential inlet.

This configuration achieved $S_N = 0.39$ but a relatively low efficiency of 93.6%, this was mainly due to the lower swirl: with the lower centrifugal acceleration the oxidizer is able to escape easily through the nozzle without combining with the fuel (Fig. 5.48, 5.50). A solution to increase turbulent mixing without increasing the swirl number was needed. Different placements and number of the fuel injectors were tried in the following configurations and the oxidizer injectors have been gradually reduced in length.

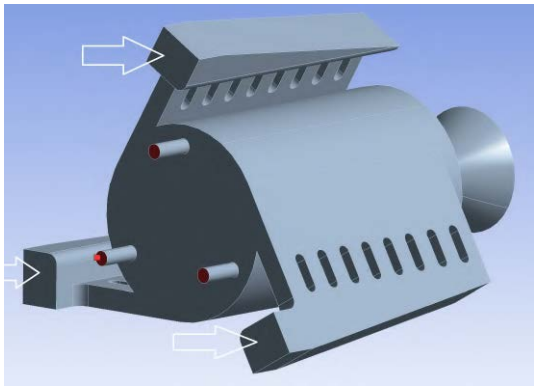

Figure 5.47: Swirl of oxidizer configuration SO1.7: injectors. Oxidizer injection planes indicated by white arrows. Fuel injection in red.

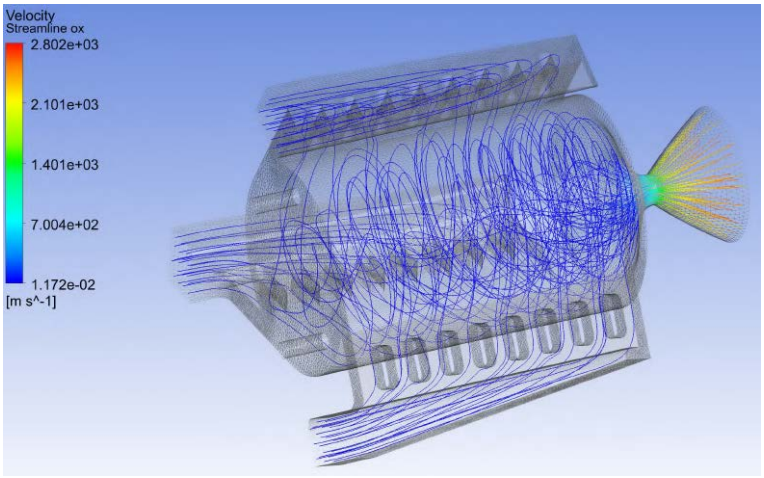

Figure 5.48: Swirl of oxidizer configuration SO1.7: streamlines. Oxidizer only.

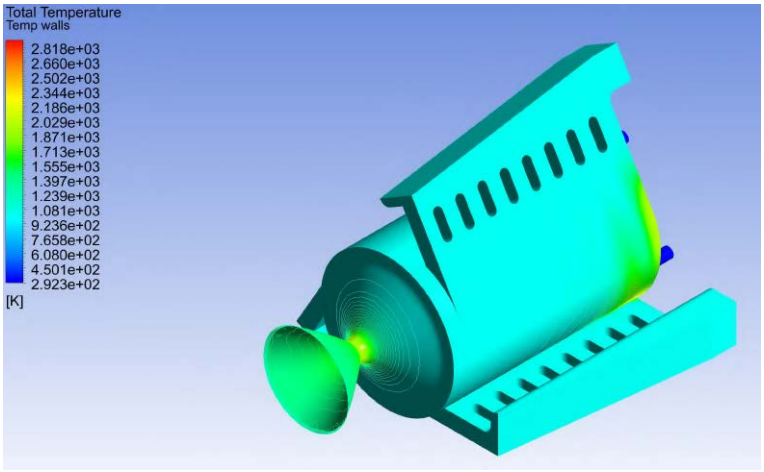

Figure 5.49: Swirl of oxidizer configuration SO1.7: total temperature of the fluid at the wall boundary.

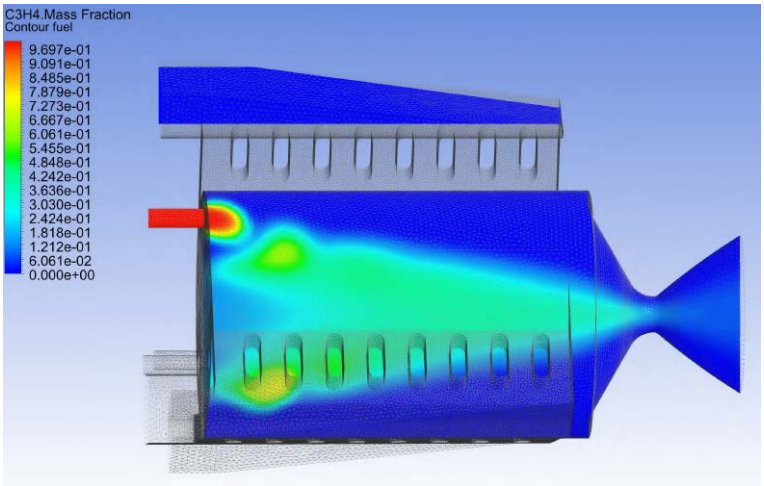

Figure 5.50: Coaxial configuration SO1.7: fuel mass fraction.

5.3.2 Swirl of oxidizer with impinging (SO2)

Having previously obtained good results with the impinging injection in the coaxial designs, it was tried on the swirling design too. With the swirling motion the impinging jets would be bent, so the circular hole design was unsuitable because the streams would probably not meet. Instead the elongated slot design was used from the beginning, to ensure the impinging jets would meet at least partially.

5.3.2.1 Best swirling configuration: SO2.1.5

This is the fifth and most performing minor revision of the SO2.1 design (6 revisions total). An impinging triplet is used with slotted inlets to help the streams meet. The main dimensions of the system are in Fig. 5.52. Compared with SO1.7 the tangential inlet has been shortened to 8 mm (part of the oxidizer flow has been redirected in the impinging injectors) and the flat bottom has been replaced by a more classical rounded divergent design.

The impinging injection divides successfully the fuel jet in two streams, each of them takes an elicoidal path when it encounters the tangentially flowing oxidizer near the side wall (Fig. 5.55, 5.56). The combustion is confined in the center of the chamber and, thanks to the shortened tangential inlets, the amount of oxidizer exiting the nozzle without reacting is minimal.

It results in a 98.9% combustion efficiency (based on pressure), with an average 1191 K total temperature at the wall boundary and 157.1 $W/(m^2K)$ convective heat transfer coefficient. From the head to the divergent part of the nozzle, the walls are more or less at the same temperature as the decomposed HTP. Swirl number in the chamber is a reasonable 0.45. The fuel mass fraction on the throat section is 1.7%.

The mesh used in this simulation featured 2.08 million elements, another one with 3.18 million elements was tested resulting in an increment of just 0.35% in chamber pressure.

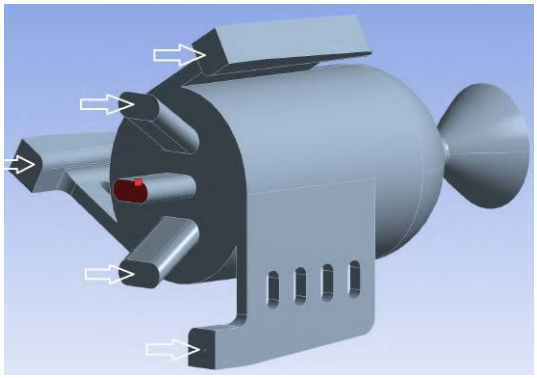

Figure 5.51: Coaxial configuration SO2.1.5: injectors. Oxidizer injection planes indicated by white arrows. Fuel injection in red.

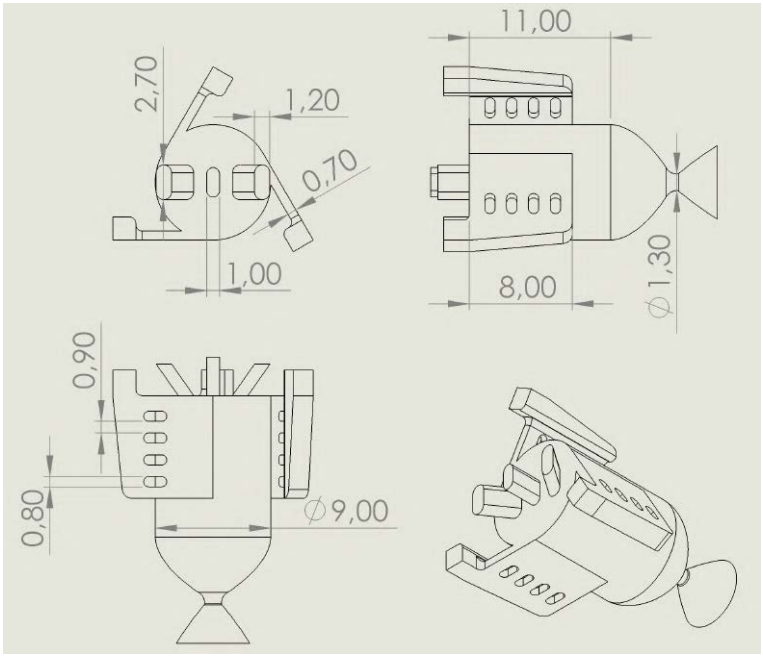

Figure 5.52: Coaxial configuration SO2.1.5: main design dimensions.

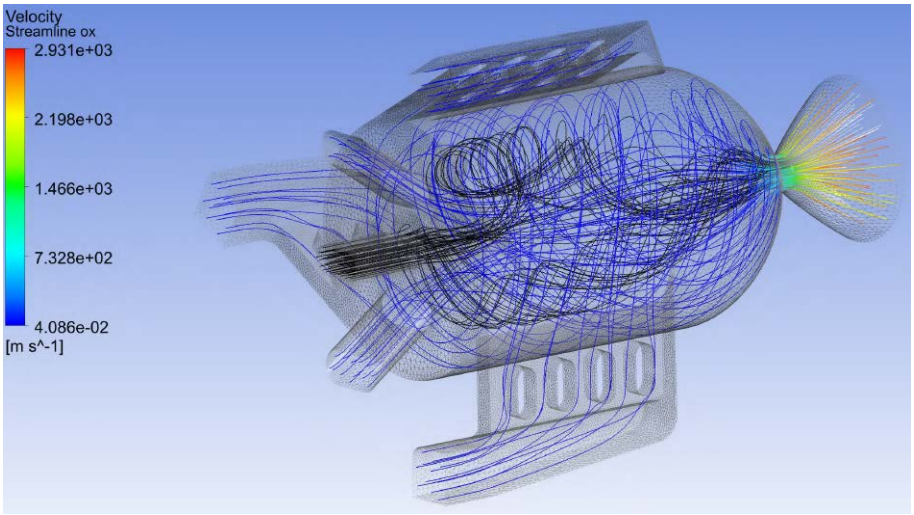

Figure 5.53: Coaxial configuration SO2.1.5: streamlines. Oxidizer is rainbow color-coded, fuel is black.

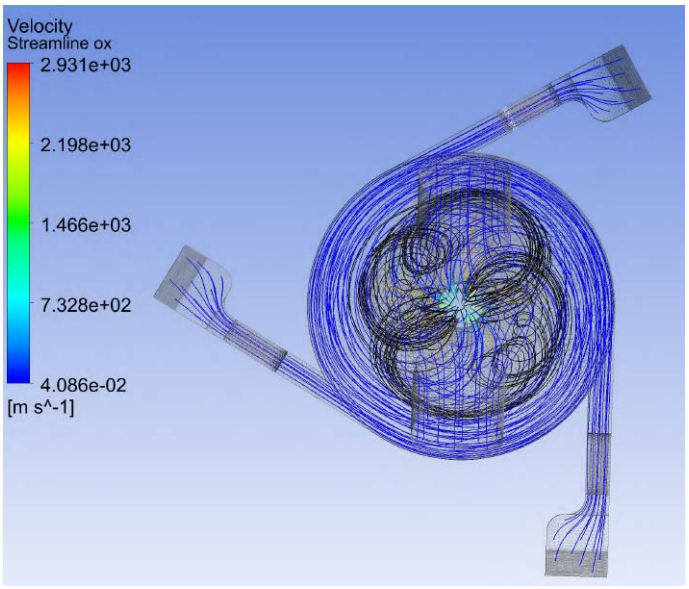

Figure 5.54: Coaxial configuration SO2.1.5: streamlines from the front. Oxidizer is rainbow color-coded, fuel is black.

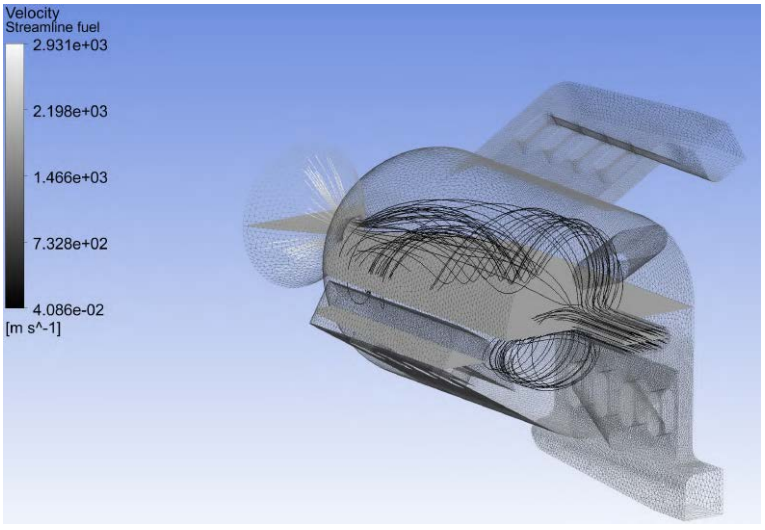

Figure 5.55: Coaxial configuration SO2.1.5: fuel streamlines. Middle plane (grey) added to ease visualization of flow.

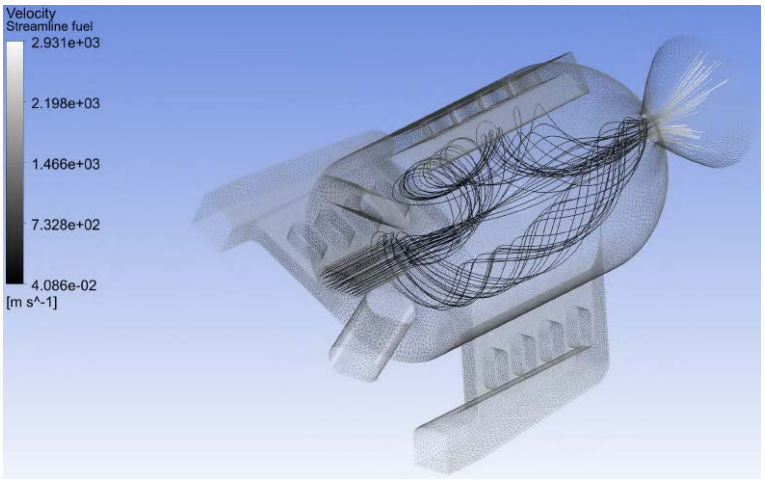

Figure 5.56: Coaxial configuration SO2.1.5: fuel streamlines.

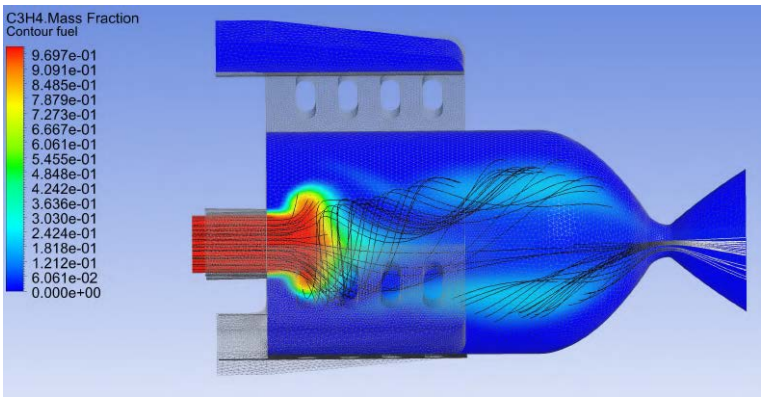

Figure 5.57: Coaxial configuration SO2.1.5: fuel mass fraction.

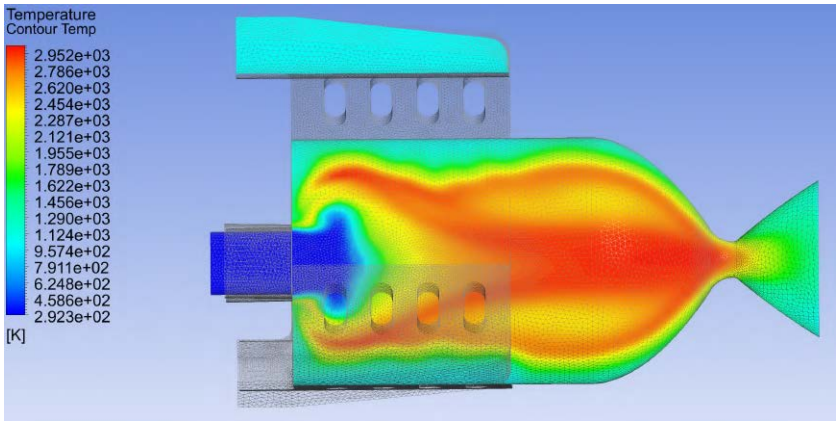

Figure 5.58: Coaxial configuration SO2.1.5: temperature profile inside the engine.

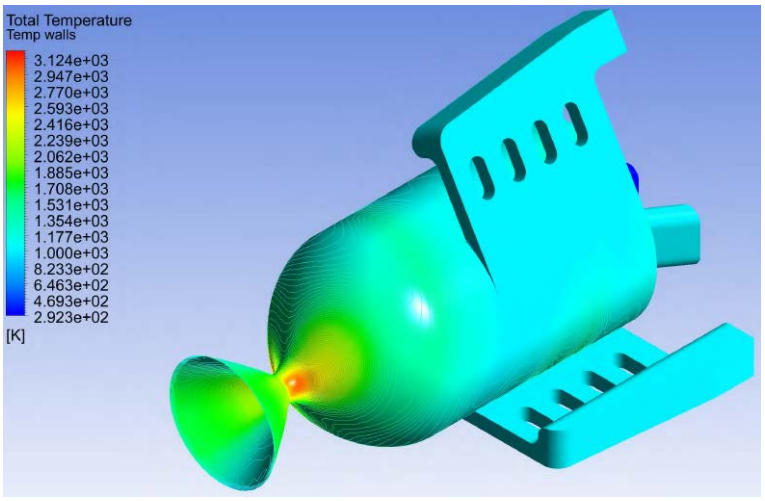

Figure 5.59: Coaxial configuration SO2.1.5: total temperature of fluid at the wall boundary.

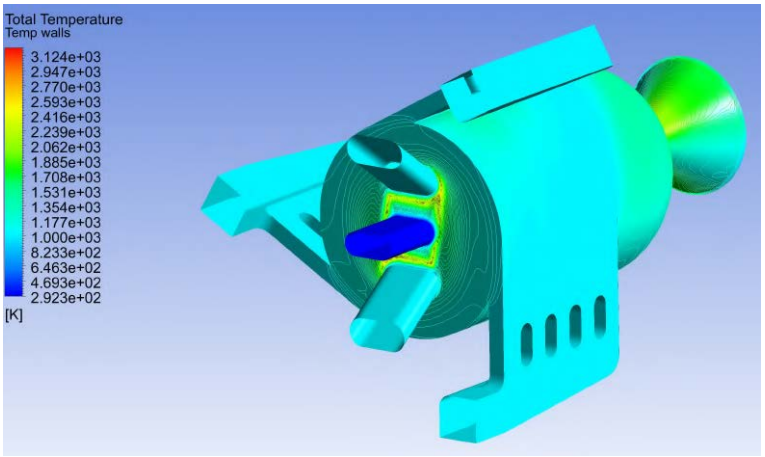

Figure 5.60: Coaxial configuration SO2.1.5: total temperature of fluid at the wall boundary. Frontal view.

5.4 Swirl of fuel series (SF)

Only 2 configurations have been tested of this kind, leading to similar underwhelming thermal results. These were again VCCW designs [24], but used fuel for tangential injection instead of oxidizer. Unfortunately the O/F=6.5 meant there was very little flow rate of fuel available compared to the oxidizer and their difference in injection temperature (and therefore density) only made things worse.

The fuel injector was set to 0.5 mm in diameter to provide the maximum possible momentum without going below the minimum additive manufacturing dimensional limit we set earlier.

The results in both the tested designs indicated the mass flow of fuel was simply not enough to create an effective film cooling of the entire side wall (Fig. 5.64), nor to induce any significant amount of swirling: SF1.1 had a $S_N = 0.03$, SF1.2 had $S_N = 0.05$, which are numbers typical for a completely non swirling design. The kinetic energy of fuel gets dissipated very quickly after injection.

Furthermore, a section view (Fig. 5.63) of SF1.1 reveals most of the internal chamber volume is wasted because all the mixing happens very close to the side wall.

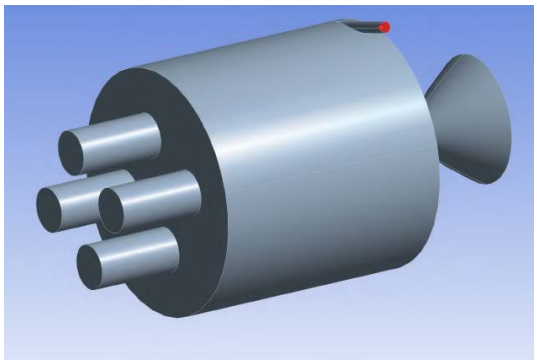

Figure 5.61: Swirl of fuel configuration SF1.1: injectors. Fuel injection in red.

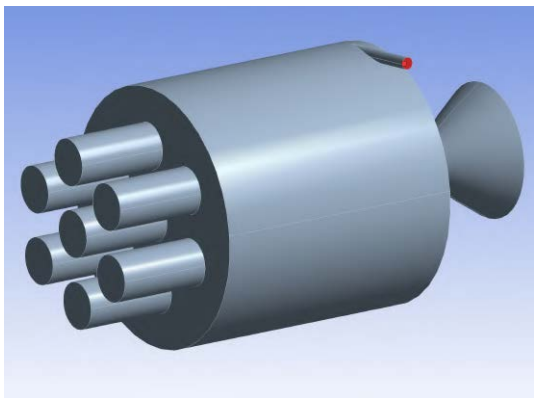

Figure 5.62: Swirl of fuel configuration SF1.2: injectors. Fuel injection in red.

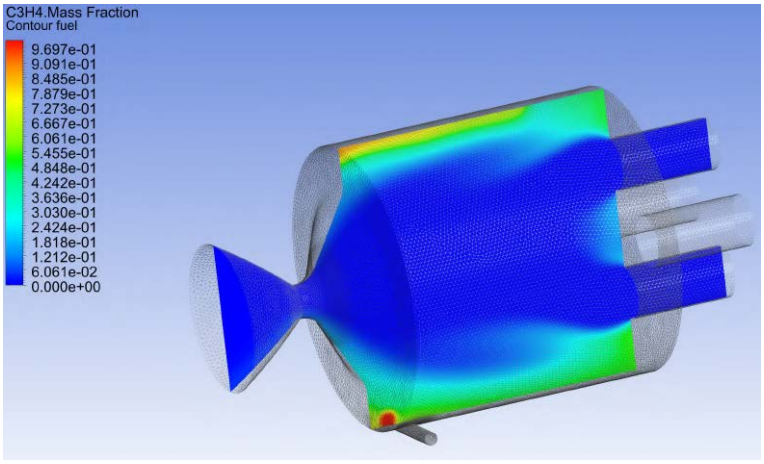

Figure 5.63: Swirl of fuel configuration SF1.1: fuel mass fraction.

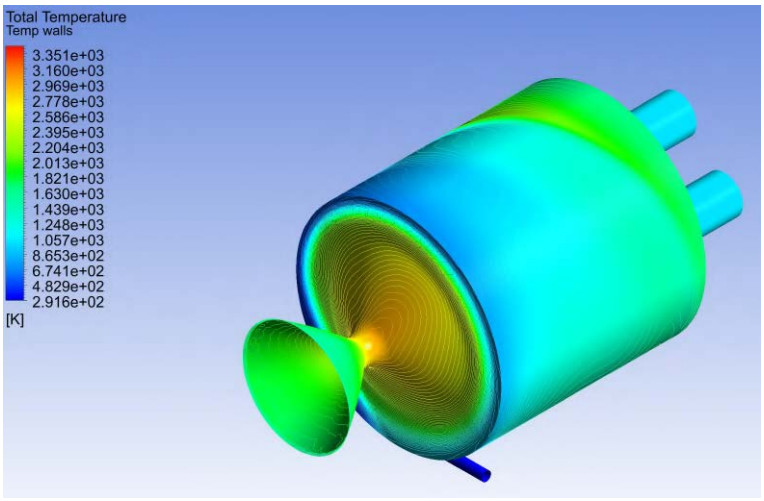

Figure 5.64: Swirl of fuel configuration SF1.1: total temperature of fluid at the wall boundary.

5.5 Comparison between C2.17 and SO2.1.5

Due to the nature of Eq. 3.2 (convective heat transfer equation), without setting a maximum wall temperature, it is impossible to know if it is more beneficial to have, at the wall boundary, a lower convective heat transfer coefficient or a lower local gas temperature. From a engineering stand point, the location also plays a crucial part: nozzles usually are protruding from the satellite, therefore radiative cooling could be feasible, while the head and side wall of the engine could need capacitive and/or regenerative cooling. It should be noted that due to the very compact size of the engine illustrated in this work, a completely radiative cooling could be a possible route if the whole combustion chamber is placed outside the satellite.

To provide a comparison of the convective heat flux expected from the two best configurations, Eq. 3.2 was used with the heat transfer coefficient from the adiabatic simulations and different hypotetical wall temperatures to get an estimate of the total heat flux on the head of the

engine and its side walls (all surfaces are calculated excluding injectors). This is just a linear approximation because the convective heat transfer coefficient is actually a function of the local fluid properties, which are in turn dependent on the fluid temperature which depend on the heat transfer. Therefore the further each point in Fig. 5.65 is from its corresponding adiabatic wall temperature (i.e. from the zero heat transfer coordinate), the more inaccurate the estimate is.

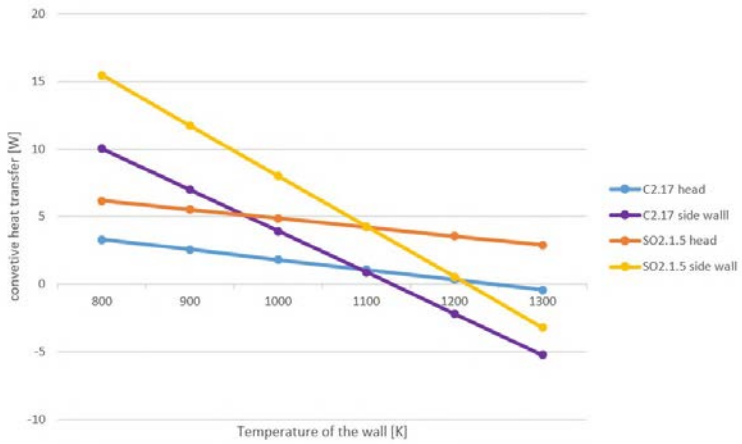

Figure 5.65: Approximation of the expected convective heat flux for the best configurations of this work.

From Table 5.1 we can see the coaxial configuration has lower convective heat transfer coefficients but higher average adiabatic wall temperatures, especially on the head surface.

Table 5.1: Near-wall heat convection data for adiabatic configurations C2.17 and SO2.1.5

	C2.17		**SO2.1.5**	
	head	side wall	head	side wall
Surface $[mm^2]$	64.4	492.4	63.8	250
Convective coeff. $[W/m^2K]$	101.4	75.8	116.3	122.2
Avg adiabatic wall temp [K]	1744	1214	1206	1089

6 Conclusion

The popularity of small-sats seen in the recent years calls for new miniaturized propulsion systems. While small cold-gas thrusters are already available, they cannot provide the delta-V necessary for more demanding missions and the market still does not have many high-performance miniaturized chemical engines.

Many issues are in the way of bipropellant chemical micro-propulsion, from safety regulations that are slightly loosening only in the recent days to the difficulties of thermal management with such a high $surface/volume$ ratio at small scales. However the path is traced and the market is clearly moving towards miniaturization and lower cost higher risk missions. Another aspect is also the replacement of few costly satellites with a large number of smaller and cheaper satellites.

A new bipropellant rocket engine with 1 N thrust with storable propellants is in the early development stage. High-Test Peroxide is the oxidizer of choice due to its storability, relatively high performance and the experience gained by the University of Padua with it.

In order to avoid the downsides of high swirl in engines, such as increased pressure at the wall boundary and restriction of the flow in the throat, the swirling designs were restricted to low swirl numbers.

In this work 2 engine designs have been found to provide very low fluid temperatures at the wall while keeping a high combustion efficiency, called C2.17 and SO2.1.5 in the previous chapters. The former features an impinging system with film cooling realized by a coaxial annular injection of oxidizer, while the latter has a tangential injection of oxidizer covering most of the side wall and an impinging triplet at the center. Both of them make use of an elongated slot shape for the impinging injectors to counter the sensitivity to manufacturing inaccuracies, typical of impinging designs.

In order to keep production costs low and minimize the number of potential failure points, the engine should be additively manufacturable, therefore some relevant design criteria have been applied to ensure that objective.

The fluid dynamics have been the main focus of this work and the choice of fuel is not definitive. Some fuel suggestions have been provided (propane, propene, propyne) and other engineering consideration must be made for a final choice (for example chemical stability and safety). Propyne has been used as the "demonstrative fuel", being the one with highest impulse density, although its stability and materials compatibility could be the reason for a different choice. Even the

oxidizer can be replaced and the chamber designs shown could be adapted for use with something different, for example with nitrous oxide. The chemical reaction has been represented as a one-step reaction estimated with the help of the thermochemical equilibrium software CPROPEP and some manual adjustments to reduce the number of species treated in the simulations.

A commercial CFD software (Ansys CFX) was used to perform the simulations using the $k - \epsilon$ eddy viscosity turbulence model, which is a fast and quite robust method that has previously shown good agreement with hybrid rocket motor tests. The combustion model was the eddy dissipation one, which is applicable to flows with fast chemical kinetics compared to the fluid turbulent time scale.

Future work should comprehend a coupled thermal fluid analysis to find the actual wall temperature distribution of the engine with a cooling system applied. After this this, structural FEA should guide the choice of the material for the engine. Finally the engine needs to be manufactured and hot fire tests are required to validate the results found with the RANS simulations in this thesis, since inaccuracies are introduced by the turbulence model of the Reynolds stress term. This was also the reason why 2 different injection designs were researched instead of just one: it increases the chances to get at least one good performing engine in real-world tests.

The results found should be considered a starting point for high performance chemical micropropulsion design, the fact this work is limited to the fluid dynamics of injection and chamber flow without hard restrictions on materials or propellants, makes it of a wider general use.

References

[1] *Space Transportation Costs: Trends in Price Per Pound to Orbit 1990-2000.* Futron Corporation, 2002.

[2] "A space-age first: A commercial craft returns from low-Earth orbit," http://edition.cnn.com/2010/US/12/08/space.flight/index.html, 2010.

[3] "Considering hydrazine-free satellite propulsion," http://www.esa.int/Safety_Security/Clean_Space/Considering_hydrazine-free_satellite_propulsion, 2013.

[4] "GeoEye-1 (OrbView-5)," http://earth.esa.int/web/eoportal/satellite-missions/g/geoeye-1, 2015.

[5] "SpaceX Makes History: Falcon 9 Launches, Lands Vertically," http://www.nbcnews.com/tech/innovation/spacex-makes-history-successfully-launches-lands-falcon-9-rocket-n483921, 2015.

[6] "CubeSats in the context of space debris," https://esamultimedia.esa.int/docs/Clean_Space/CubeSats_in_the_context_of_space_debris.pdf, 2017.

[7] "RACE double CubeSat mission," http://www.esa.int/ESA_Multimedia/Images/2019/06/RACE_double_CubeSat_mission, 2019.

[8] "Sweating the Small Stuff: CubeSats Swarm Earth Orbit," http://www.scientificamerican.com/article/sweating-the-small-stuff-cubesats-swarm-earth-orbit/, 2019.

[9] "CubeSat Propulsion Module," https://www.dawnaerospace.com/products/p/cubesat-propulsion-module, 2020.

[10] "Mars Cube One (MarCO)," http://www.jpl.nasa.gov/cubesat/missions/marco.php, 2020.

[11] "Meet Rocket Lab's Electron rocket!" http://www.rocketlabusa.com/assets/Uploads/RL-EducationGraphics-About-Rocket-Lab-and-Electron.pdf, 2020.

[12] "Planet MAPPING AND GIS," https://www.planet.com/markets/mapping/, 2020.

[13] "PlanetScope," http://spacedata.copernicus.eu/planetscope, 2020.

[14] "RapidEye Constellation to be Retired in 2020," http://www.planet.com/pulse/rapideye-constellation-to-be-retired-in-2020/, 2020.

[15] "WATER-BASED PROPULSION," https://www.tethers.com/propulsion-system/, 2020.

[16] "Who owns our orbit: Just how many satellites are there in space?" https://www.weforum.org/agenda/2020/10/visualizing-easrth-satellites-sapce-spacex/, 2020.

[17] "A 21st Century Space Capsule," http://www.boeing.com/space/starliner/, 2021.

[18] "Nanosats Database," http://www.nanosats.eu/, 2021.

[19] "National Institute of Standards and Technology Web Book," http://webbook.nist.gov/chemistry/name-ser/, 2021.

[20] "National Library of Medicine," http://pubchem.ncbi.nlm.nih.gov/source/hsdb/2508#section=Hazardous-Reactivities-and-Incompatibilities-(Complete), 2021.

[21] "Space debris by the numbers," http://www.esa.int/Safety_Security/Space_Debris/Space_debris_by_the_numbers, 2021.

[22] "Space Launch Report: Virgin Orbit LauncherOne Data Sheet," http://www.spacelaunchreport.com/launcherone.html, 2021.

[23] N. Bellomo, M. Lazzarin, F. Barato, A. Bettella, D. Pavarin, and M. Grosse, "Investigation of effect of diaphragms on the efficiency of hybrid rockets," *Journal of Propulsion and Power*, vol. 30, no. 1, pp. 175–185, 2014.

[24] M. Chiaverini, M. Malecki, J. Sauer, W. Knuth, and C. Hall, *Vortex Combustion Chamber Development For Future Liquid Rocket Engine Applications.* [Online]. Available: https://arc.aiaa.org/doi/abs/10.2514/6.2002-4149

[25] M. Chiaverini, J. Sauer, and S. Munson, *Laboratory Characterization of Vortex-Cooled Thrust Chambers for Methane/O2 and H2/O2.*

[26] N. Chigier and J. Beér, "Velocity and static-pressure distributions in swirling air jets issuing from annular and divergent nozzles," *Journal of Basic Engineering*, vol. 86, pp. 788–796, 1964.

[27] J. Cornelisse, H. Schöyer, and K. Wakker, *Rocket Propulsion and Spaceflight Dynamics*, ser. Aerospace Engineering Series. Pitman, 1979.

[28] S. Enterprise, *Nano/microsatellite market forecast, 10th edition.* SpaceWorks Enterprise, 2020.

[29] R. Humble, *Space Propulsion Analysis and Design.* McGraw-Hill Companies,Incorporated, 1995.

[30] D. Huzel, *Modern Engineering for Design of Liquid-Propellant Rocket Engines*, ser. Ingenieria de transportes y aeronautica. American Institute of Aeronautics & Astronautics, 1992.

[31] A. Inc., *ANSYS CFX-Solver Theory Guide.*

[32] N. C. L. Initiative, *CubeSat101 Basic Concepts and Processes for First-Time CubeSat Developers.* NASA, 2017.

[33] S. W. Janson, "25 years of small satellites," *25th AIAA/USU Annual Conference on Small Satellites*, 2011.

[34] A. Johnstone, "Cubesat design specification," 2021.

[35] D. J. Kessler and B. G. Cour-Palais, "Collision frequency of artificial satellites: The creation of a debris belt," *JGR: Space Physics*, 1978.

[36] O. Krauss, "Design and test of a lab-scale n2o/htpb hybrid rocket," 01 2003.

[37] K. K. Kuo and M. J. Chiaverini, *Fundamentals of Hybrid Rocket Combustion and Propulsion.* American Institute of Aeronautics and Astronautics, Inc., 2007.

[38] K. Lemmer, "Propulsion for cubesats," *Acta Astronautica*, vol. 134, 2017.

[39] P. K. Martin, *NASA's management of crew transportation to the International Space Station.* National Aeronautics and Space Administration - Office of Inspector General, 2019.

[40] J. Mueller, R. Hofer, and J. Ziemer, "Survey of propulsion technologies applicable to cubesats," 2010.

[41] NASA, *The Vision for Space Exploration.* National Aeronautics and Space Administration, 2004.

[42] J. N. Pelton, *The New Gold Rush - Riches of space beckon!* Springer, 2017.

[43] S. Pope, P. Eccles, S. Pope, and C. U. Press, *Turbulent Flows*. Cambridge University Press, 2000.

[44] J. Páscoa, O. Teixeira, and G. Ribeiro, "A review of propulsion systems for cubesats," 07 2018.

[45] N. Qayyum, S. Ghuffar, H. M. Ahmad, A. Yousaf, and I. Shahid, "Glacial Lakes Mapping Using Multi Satellite PlanetScope Imagery and Deep Learning," *International Journal of Geo-Information*, 2020.

[46] G. V. R. RAO, "Exhaust nozzle contour for optimum thrust," *Journal of Jet Propulsion*, vol. 28, no. 6, pp. 377–382, 1958.

[47] R. B. Roger Pielke Jr, "Shuttle programme lifetime cost," *Nature*, 2011.

[48] H. Sheen, W. Chen, S. Jeng, and T. Huang, "Correlation of swirl number for a radial-type swirl generator," *Experimental Thermal and Fluid Science*, vol. 12, no. 4, pp. 444–451, 1996.

[49] G. Sutton and O. Biblarz, *Rocket Propulsion Elements*. Wiley, 2016.

[50] S. M. Tieze, L. C. Liddell, S. R. S. Maria, and S. Bhattacharya, "Biosentinel: A biological cubesat for deep space exploration," *Astrobiology, April 2020*, 2020.

[51] A. R. Tummala and A. Dutta, "An overview of cube-satellite propulsion technologies and trends," *Aerospace*, vol. 4, no. 4, 2017.